Date of publication xxxx 00, 0000, date of current version xxxx 00, 0000.
Digital Object Identifier XX.XXXX/YYY.20XX.ZZZZZZZ

Linear-Rotary Position Control System with Enhanced Disturbance Rejection for a Novel Total Artificial Heart

ROSARIO V. GIUFFRIDA[1], (Student, IEEE), ANDREAS HORAT[1], DOMINIK BORTIS[1], (Senior Member, IEEE), TIM BIEREWIRTZ[2], KRISHNARAJ NARAYANASWAMY[3], MARCUS GRANEGGER[3], and JOHANN W. KOLAR[1], (Fellow, IEEE).

[1]Power Electronic Systems Laboratory, ETH Zurich, Zurich, Switzerland
[2]Deutsches Herzzentrum der Charité, Institute of Computer-assisted Cardiovascular Medicine, Berlin, Germany
[3]Department of Cardiac Surgery, Medical University of Vienna, Vienna, Austria

Corresponding author: Rosario V. Giuffrida (e-mail: giuffrida@lem.ee.ethz.ch).

ABSTRACT A novel implantable total artificial heart, hereinafter referred to as the *ShuttlePump*, is currently under development in a research collaboration between the Medical University of Vienna, the Power Electronic Systems Laboratory of ETH Zurich and Charite Berlin. Its novel, low-complexity, pulsatile pumping principle requires a specially-shaped piston performing a controlled, synchronized linear-rotary motion while providing the necessary hydraulic force and torque. The machine design of the PMSM-based linear-rotary actuator was conducted in previous work of the authors, leading to the construction of a hardware prototype satisfying the application requirements in terms of electromechanical force, torque, power losses and volume. This paper provides the details of the closed-loop linear-rotary position control system required to operate the *ShuttlePump*. The design of the position control system targets tight reference tracking ($\pm 8\,\mathrm{mm}$ linear stroke and continuous rotation) up to an operational frequency of $5\,\mathrm{Hz}$, under the heavy disturbance introduced by the axial hydraulic load force, as high as $45\,\mathrm{N}$. The experimental measurements show successful linear-rotary position tracking under the specified axial load, with a maximum error of $1\,\mathrm{mm}$ and $5°$.

INDEX TERMS Artificial biological organs, permanent magnet machines, rotating machines

I. INTRODUCTION

Mechanical Circulatory Support (MCS) devices have gained an increasingly important, life-saving role in the long-term treatment of end-stage heart failure patients [1]–[3]. In fact, with the constantly rising number of patients, expected to exceed 70 millions by 2030 [4], the demand for heart transplantations exceeds the number of available donor organs [5], [6]. Among the MCS devices of most success, Left Ventricular Assist Devices (LVADs) and Total Artificial Hearts (TAHs) have been developed, some of which are clinically available for long-term implantation. These devices are ultimately blood pumps, differing in pumping principles and designs. What they have in common is that, in order to operate properly, they inevitably need feedback control. For rotary blood pumps, for instance, the angular speed of the impeller needs to be controlled to guarantee a specified flow rate [7], [8]. Similarly, some positive displacement blood pumps make use of a controlled linear motion to push the blood into circulation [9], [10]. Finally, the most advanced blood pumps featuring active magnetic bearings strictly rely on stable position control of the levitated impeller [11], [12]. MCS devices have dedicated power and control units that include a battery pack (typically with more than a single battery) for power supply. They are used not only to maintain the operating conditions of the pump, but also for monitoring, fault detection, and alarm raising. For implantable devices, the units are extra-corporeal and connected via a percutaneous driveline, although the use of trans-cutaneous energy transfer systems has risen increased interest in recent years [13]. In this context, the novel implantable TAH *ShuttlePump* (cf. **Fig. 1 (a)**) is an eloquent example of the importance of feedback control in enabling blood pumping operation. The *ShuttlePump* is currently under development in a research collaboration between *Charité Berlin*, the *Medical University of Vienna* and the Power Electronic Systems Laboratory of ETH Zurich [14]–[17]. The key peculiarity of this device resides in its pumping principle, which requires only one moving part to provide a pulsatile, physiological blood flow. In contrast, pulsatile-flow blood pumps typically feature mechanical valves or membranes, which are not only prone to

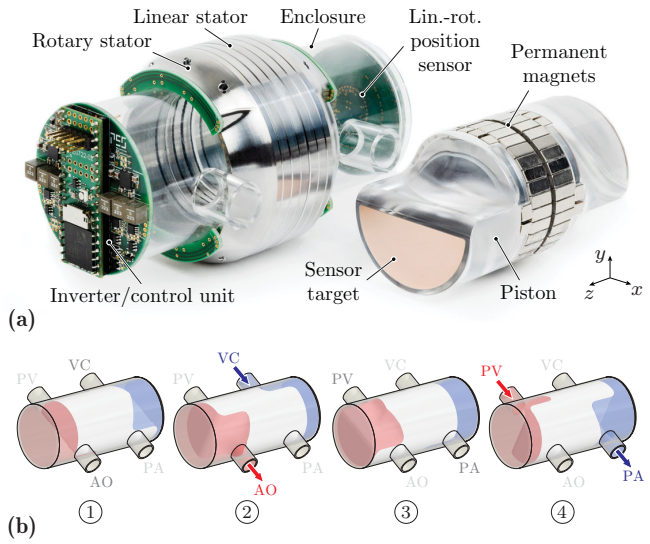

FIGURE 1. **(a)** Prototype of the Linear-Rotary Actuator (LiRA) for the implantable Total Artificial Heart (TAH) *ShuttlePump*, including the LiRA stator, PCB-based eddy-current position sensors, compact inverter/control unit and moving piston with embedded Permanent Magnets (PMs) and copper sensor targets. **(b)** Operating principle of the *ShuttlePump*. The piston continuously rotates around the z-axis, controlling opening/closing of the inlets/outlets and establishing a hydrodynamic journal bearing. During the left systole (stages 1 and 2), the piston translates along the positive z-axis, pushing the blood in the left chamber out while the right chamber fills up. During the right systole (stages 3 and 4), the translation direction is reversed, as well as the chambers being emptied/filled up.

fail, but also increase the chances of thrombotic formations within the pump. The *ShuttlePump* uses instead a specially-shaped piston, following a combined low-frequency linear-rotary motion. This allows providing a pulsatile flow with low blood damage and without the need for valves. While the linear motion causes the blood to be pushed into circulation, the rotary motion controls the opening and closing of the inlets and outlets of the pump. In addition, with a constant rotation, the piston can support itself radially while immersed in blood by establishing a hydrodynamic journal bearing. Therefore, the need for synchronized linear-rotary position control, compliant to the required hydrodynamic force and torque is apparent. Previous work of the authors at *Charité Berlin* and the *Medical University of Vienna* covered the fluid-dynamic, clinical and physiological aspects of the *ShuttlePump*, leading to the definition of the pump concept [14], [15]. At the Power Electronic Systems Laboratory of ETH Zurich, the challenging task of defining an appropriate actuation and sensing concept, under the stringent requirements/constraints of the system (such as limited volume, mass and power losses) was tackled. This led to the design, realization and experimental verification of the compact PMSM-based Linear-Rotary Actuator (LiRA) [16], [17] and the integrated eddy-current-based linear-rotary position sensors [18]. This paper represents a point of arrival in the development of the complete *ShuttlePump* drive system. The realized LiRA prototype is complemented with its inverter and control unit, on which the closed-loop linear-rotary position control system is implemented.

This paper is structured as follows. **Sec. II** gives a brief overview of the *ShuttlePump* and its drive system, summarizing its operating principle, the characteristics of the realized LiRA, and defining the motion control requirements. In **Sec. III**, the derivation of an electro-mechanical dynamical model for the LiRA of *ShuttlePump* is presented. This is used in **Sec. IV** to design the cascaded current and linear-rotary position control systems. The hardware implementation of the entire system is then discussed in **Sec. V**. The experimental verification with the LiRA operated in closed-loop follows in **Sec. VI**. Finally, **Sec. VII** concludes the paper.

II. SHUTTLEPUMP TAH AND LIRA DRIVE SYSTEM

This section provides a compact overview of the *ShuttlePump* and the parts of its drive system. After summarizing its operating principle, the previously realized LiRA and linear-rotary position sensors are briefly described. Finally, the motion control requirements are defined.

A. OPERATING PRINCIPLE, DIMENSIONS AND REQUIREMENTS

A thorough explanation of the pumping principle of the *ShuttlePump* is given in previous work from the authors [14], [15]. Therefore, in the following only the most relevant details are summarized. As shown in the 3D cut view of **Fig. 2**, the *ShuttlePump* consists of a cylindrical enclosure with two blood chambers serving as left and right ventricles. Each chamber has an inlet and an outlet and is separated from the other by the specially-shaped piston. The position of the piston needs to be precisely and simultaneously controlled both in the axial and circumferential directions, in order to guarantee proper pumping operation. In particular, as illustrated in **Fig. 1 (b)**, the axial/linear motion is needed to pump the blood out of one chamber, while the other one fills with new blood. The circumferential/rotary motion, together with the special shape of the piston, controls the opening/closing of the inlets/outlets of the enclosure, removing the need for any valve. Additionally, by continuous rotation at a frequency of at least $1.5\,\mathrm{Hz}$, a hydrodynamic journal bearing is established, which supports the piston radially during operation. The operational frequency needs to be the same both for the linear (shuttling) and rotary motion, and is at most $f_{\mathrm{op,max}} = 5\,\mathrm{Hz}$. The drive system enabling such operation needs to comply with several limitations and requirements. **Tab. 1** reports the most important ones, which guided the design of the LiRA. The main challenge is to respect the axial force requirement of $F_{\mathrm{req,max}} = 43\,\mathrm{N}$ during linear motion, with the least ohmic losses and in the least volume. Continuous ohmic losses significantly above the specified limit $P_{\mathrm{Cu,avg,max}} = 10\,\mathrm{W}$ would result in blood damage, which is the reason why the standards for implantable devices prescribe a maximum temperature increase of $\Delta T_{\mathrm{max}} = 2\,\mathrm{K}$ of the body temperature. An actuator volume above the specified outer dimensions would instead impair the implantability of the *ShuttlePump*.

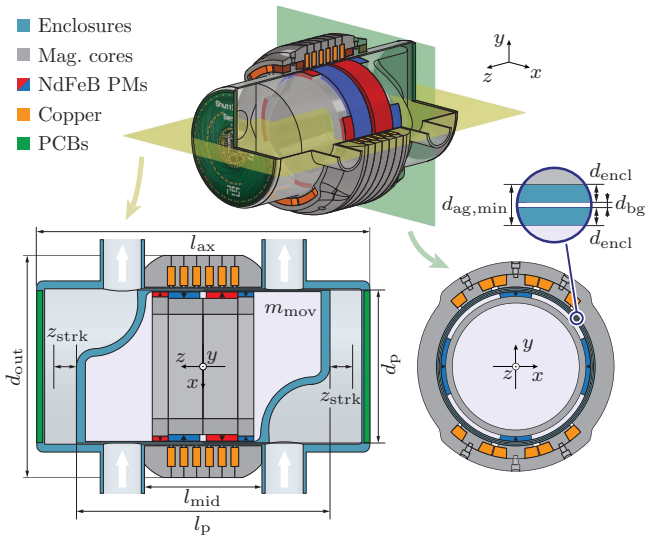

FIGURE 2. Sectional (xy- and yz-) views of the *ShuttlePump*, showing its enclosure and specially-shaped piston with annotated dimensions, reported in **Tab. 1**. Also the designed LiRA is visible, consisting of linear and rotary stators (around the enclosure) and the moving part with NdFeB permanent magnets, i.e., the *mover*, which is embedded in the piston [16], [17].

TABLE 1. Specifications of the *ShuttlePump* (cf. **Fig. 2**), reported from [17].

Name	Symbol	Value	Unit
Maximum axial dimensions	l_{ax}	105	mm
Maximum radial dimensions	d_{out}	70	mm
Piston axial length	l_p	78	mm
Piston outer diameter	d_p	48.72	mm
Inter- in-/outlets distance	l_{mid}	40	mm
Inlet/outlet diameter	d_{io}	12	mm
Enclosure thickness (lateral)	d_{encl}	0.5	mm
Blood gap	d_{bg}	140	um
Magnetic gap	$d_{ag,min}$	1	mm
Axial stroke amplitude	z_{strk}	8	mm
Maximum axial force	$F_{req,peak}$	≈ 43	N
Axial torque	M_{req}	3.1	mN m
Maximum radial force	$F_{rad,max}$	25	N
Piston weight	m_{mov}	< 300	g
Piston frequency	f_{op}	1.5 - 5	Hz
Piston rotational speed	Ω_{op}	90 - 300	rpm
Max. speed ripple (open loop)	$\Delta\Omega_{op}$	< 20	%
Operating conditions		2.5 - 9	L/min
Max. average cont. losses	$P_{Cu,avg,max}$	10	W
Blood temperature increase	ΔT_{max}	2	K

B. REALIZED LIRA AND LINEAR-ROTARY POSITION SENSORS

The LiRA of the *ShuttlePump* consists of two distinct functional parts, i.e., the Linear Actuator (LA) and the Rotary Actuator (RA). The analysis, design and experimental verification of the LA and the RA are available and discussed in detail in previous work from the authors [16], [17]. For the sake of completeness, a summary with the main characteristics of the LiRA can be found in the **Appendix A**. The moving part of the LiRA (equipped with permanent magnets) is hereinafter denoted as '*mover*', whereas the term '*piston*' refers to the complete mechanical element of the *ShuttlePump*. As the mover is rigidly embedded in the piston, the linear and rotary positions of the piston will be equivalently denoted as z_{mov} and φ_{mov}. The LiRA parameters that are relevant for the subsequent electro-mechanical system modeling and feedback control are reported in **Tab. 2**. The winding of the LA consists of 6 circular coils with resistance $R_{c,lin} = 2.2\,\Omega$ and inductance $L_{c,lin} = 4.7\,\text{mH}$. For each phase, 2 coils are connected in antiseries. Therefore, in the following sections, the total phase resistances $R_{lin} = 2 \cdot R_{c,lin}$ and inductance $L_{lin} = 2 \cdot L_{c,lin}$ are considered for the LA. The winding of the RA instead consists of 12 concentrated coils with resistance $R_{c,rot} = 6.4\,\Omega$ and inductance $L_{c,rot} = 6.9\,\text{mH}$. With 4 coils per phase, $R_{rot} = 4 \cdot R_{c,rot}$ and $L_{rot} = 4 \cdot L_{c,rot}$ are considered. The measured machine constants [16], [17] are reported in **Fig. 3**. On average, the force and torque constants are $k_{LA} = 22.9\,\text{N A}^{-1}$ and $k_{RA} = 33.3\,\text{mN m A}^{-1}$, respectively. The phase flux linkages $\psi_{\{a,b,c\},\{lin,rot\}}$ for the LA and the RA are extracted from FEM simulations and

TABLE 2. Parameters of the realized *ShuttlePump* LiRA.

Name	Symbol	Value	Unit
Mover mass	m_{mov}	0.248	kg
Linear friction coefficient	b_{lin}	1	$\text{N m}^{-1}\,\text{s}$
Mover moment of inertia	J_{mov}	70	kg m^2
Rotary friction coefficient	b_{rot}	10^{-4}	$\text{N m rad}^{-1}\,\text{s}$
Phase resistance (LA)	R_{lin}	$2 \cdot 2.2$	Ω
Phase inductance (LA)	L_{lin}	$2 \cdot 4.7$	mH
Phase resistance (RA)	R_{rot}	$4 \cdot 6.4$	Ω
Phase inductance (RA)	L_{rot}	$4 \cdot 6.9$	mH
Force constant	k_{LA}	**Fig. 3 (a)**	N A^{-1}
Torque constant	k_{RA}	**Fig. 3 (b)**	mN m A^{-1}
Pole pitch (LA)	τ_{pp}	24	mm
Pole pairs (RA)	P	4	
Peak flux linkage (LA)	$\hat{\Psi}_{PM,lin}$	70	mWb
Peak flux linkage (RA)	$\hat{\Psi}_{PM,rot}$	7.3	mWb
LC filter inductance	L_f	22	µH
LC filter capacitance	C_f	10	µF
LC filter damping resistance	R_f	2	Ω

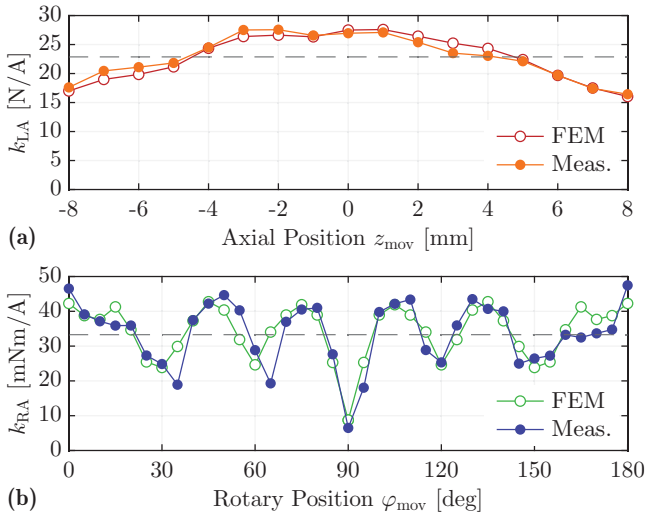

FIGURE 3. Measured machine constants, compared to the simulated values from FEM, for **(a)** the LA and **(b)** the RA. Both exhibit a position dependency due to the motor characteristics [16], [17]. On average, $k_{LA} = 22.9\,\text{N A}^{-1}$ and $k_{RA} = 33.3\,\text{mN m A}^{-1}$.

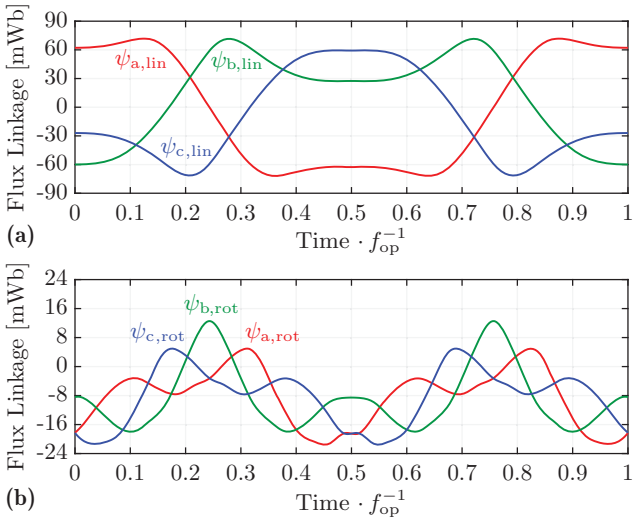

FIGURE 4. Simulated phase flux linkages $\psi_{\{a,b,c\},\{lin,rot\}}$ for **(a)** the LA and **(b)** the RA for a cycle of operation with frequency $f_{op} = \{1.5, \ldots, 5\}$Hz.

reported in **Fig. 4**. To control the motion of the piston, it is necessary to complement the LiRA with linear-rotary position sensors. Their eddy-current-based design was already covered in previous work [18]. For completeness, further information is provided in the **Appendix B**. Two linear-rotary position sensors are used, placed on the two sides of the enclosure. The measured sensor signals are post-processed with a linear weighting according to the axial position of the piston, as further explained in **Appendix C**. This is done to use the information from the sensor that is closer to its target, for which the measurement signals have better quality (higher sensitivity, less noise). The measurement bandwidth is $f_{sens} = 10$ kHz, which is largely sufficient and hence does not introduce significant delays to be considered during the design of the controller.

C. MOTION CONTROL REQUIREMENTS FOR THE LIRA

Concluding the overview of the *ShuttlePump*, it is important to briefly pinpoint the motion control requirements that guide the following linear-rotary position control design. The specified motion profile for the piston is shown in **Fig. 5 (a-b)**. Synchronization of the axial/linear position z_{mov} with the angular/rotary position φ_{mov} is essential. In fact, the pump operates correctly if the blood is pushed out of one chamber only when its inlet is closed and its outlet opened. To guarantee that this condition is respected with the given piston and enclosure geometry, the piston holds its axial position for a short time interval t_{hold} at the two edge positions $z_{mov} = \pm z_{strk}$, while the rotation continues (cf. **Fig. 5 (a-b)**). The duration of the hold interval depends on the operational frequency as

$$t_{hold} = \frac{\varphi_{hold}}{360°} \frac{1}{f_{op}}, \tag{1}$$

where φ_{hold} is the rotary angle to be traveled during the hold phase, which is strictly linked to the rotary positioning accuracy.

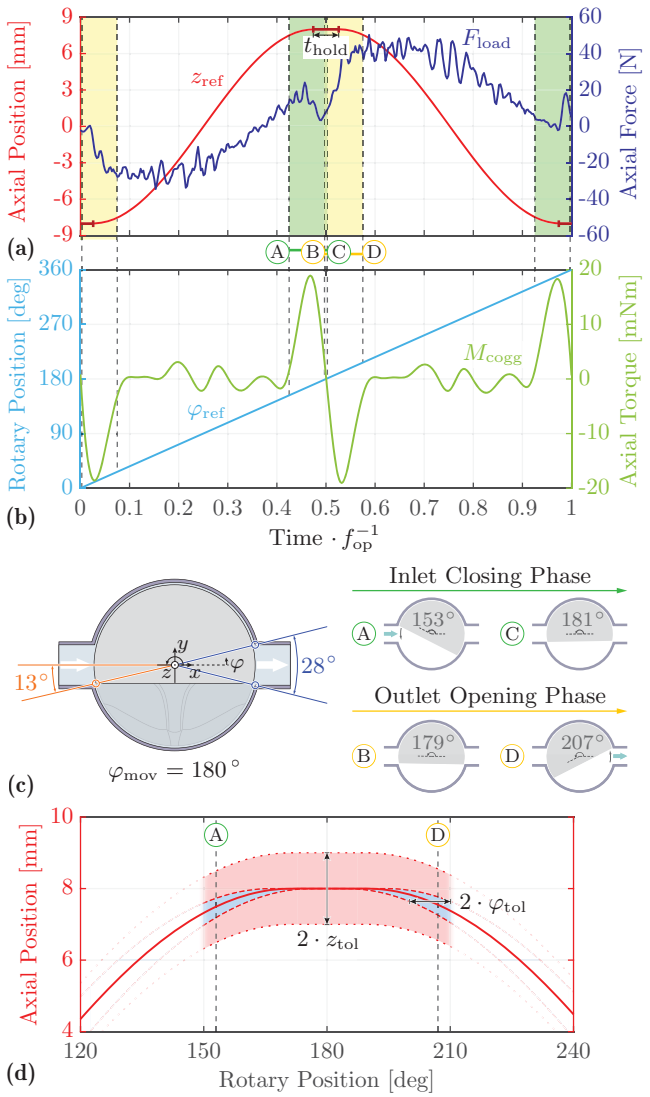

FIGURE 5. **(a)** Sectional view of the *ShuttlePump* for the case $\varphi_{mov} = 180°$. According to the given geometry of the piston and the highlighted angles, the inlet closing phase and the outlet opening phase are defined. **(b-c)** Specified linear and rotary motion profile of the *ShuttlePump*, with force and torque requirements. Both motions have to be synchronized and tracked in the operational range $f_{op} = \{1.5, \ldots, 5\}$Hz. The hydraulic load force F_{load} and the cogging torque M_{cogg} are the main disturbances to be rejected by the position control system. The inlet closing phase and the outlet opening phase are highlighted in green and yellow, respectively. **(d)** Axial-rotary position diagram with highlighted tolerance bands. The control error boundaries $z_{tol} = 1$ mm and $\varphi_{tol} = 5°$ should be respected tightly in the range $\varphi_{mov} = [153°, 207°]$.

To understand how φ_{hold} can be selected, consider the sectional view of **Fig. 5 (c)**. With a diameter of $d_{io} = 12$ mm, a single inlet/outlet spans 28° along the inner circumference of the enclosure. When the piston blade lies horizontally, i.e., for $\varphi_{mov} = \{0, 180\}°$, it occludes an angle of 27° in front of both the inlet and the outlet, as the angle to the flat edge of the blade is 13°. For the sake of simplicity, consider only the case $\varphi_{mov} = 180°$ illustrated in **Fig. 5 (c)** (the case $\varphi_{mov} = 0°$ is analogous). With the given geometry and angles, it is possible to define the *inlet closing phase* over the range $\varphi_{mov} = [153°, 181°]$, and the *outlet opening phase*

over the range $\varphi_{\mathrm{mov}} = [179°, 207°]$. There is two cases for which the pumping operation could be incorrect if no hold interval is introduced:

- in case of a pronounced *lag* in the rotational position, when the direction of the linear motion of the piston inverts, the blood is pushed out of the chamber through the still open inlet, as the outlet is still closed;
- in case of a pronounced *lead* in the rotational position, when the direction of the linear motion of the piston inverts, the blood is drawn into the chamber through the already open outlet, as the inlet is already closed.

With $\varphi_{\mathrm{hold}} = 2 \cdot 10°$, i.e., with a symmetric plateau in the axial position over 20° of rotation in the range $\varphi_{\mathrm{mov}} = [170°, 190°]$, a maximum rotary position lead/lag (or maximum absolute rotary position error) of $\varphi_{\mathrm{err,max}} = 9°$ can be tolerated without compromising the pumping operation.

It should be further considered that $\varphi_{\mathrm{err,max}}$ consists of two components, namely a control component $\varphi_{\mathrm{err,contr}} = \varphi_{\mathrm{ref}} - \varphi_{\mathrm{meas}}$ due to the tracking performance of the rotary position controller and a measurement component $\varphi_{\mathrm{err,meas}} = \varphi_{\mathrm{meas}} - \varphi_{\mathrm{mov}}$ given by the sensor accuracy. In total, $\varphi_{\mathrm{err,max}} = |\varphi_{\mathrm{err,contr,max}}| + |\varphi_{\mathrm{err,meas,max}}|$ in the worst case. Considering that the sensor introduces already $|\varphi_{\mathrm{err,meas,max}}| = 4°$ [18], the specification on the tracking error for the rotary position controller is set to $\varphi_{\mathrm{tol}} = |\varphi_{\mathrm{err,contr,max}}| = 5°$. As indicated in **Fig. 5 (d)**, this specification should be respected tightly in the ranges $\varphi_{\mathrm{mov}} = [153°, 207°]$ and $\varphi_{\mathrm{mov}} = [0°, 27°] \cup [333°, 360°]$, i.e., from the beginning of the inlet closing phase till the end of the outlet opening phase. Finally, it should be observed that, if necessary, it is always possible to extend the duration of t_{hold} to accommodate for larger rotary positioning inaccuracies. However, this results in a sharper linear motion profile with higher acceleration, which requires a slightly higher current and hence ohmic losses in the LA.

For the linear motion, the main requirement on the tracking of the quasi-sinusoidal motion profile is that the piston does not hit the axial ends of the enclosure. As a safety margin of $3\,\mathrm{mm}$ between piston and enclosure at the two edge positions $z_{\mathrm{mov}} = \pm z_{\mathrm{strk}}$ is already considered in the dimensions of the *ShuttlePump*, the maximum tracking error for the linear position controller is set to $z_{\mathrm{tol}} = |z_{\mathrm{err,contr,max}}| = 1\,\mathrm{mm}$. This specification should be met particularly around the plateau phase (cf. **Fig. 5 (d)**).

III. ELECTRO-MECHANICAL SYSTEM MODELING

This section introduces the electro-mechanical model [19]–[21] of the *ShuttlePump* LiRA. First, the mechanical linear and rotary dynamic subsystems are derived and linearized. The radial dynamics of the piston is not considered, as it is stabilized by the hydrodynamic journal bearing. Then, the electrical subsystem describing the phase currents of the LiRA in the mover-oriented frame is introduced. Note that in the following, in order to keep the notation simple, the dependency on time t is not explicitly indicated.

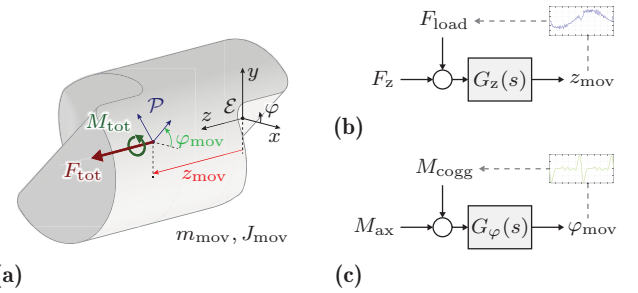

FIGURE 6. **(a)** Free-body diagram of the piston of the *ShuttlePump*, with enclosure ($\mathcal{E}$) and piston ($\mathcal{P}$) reference frames. The piston linear-rotary motion is described with respect to the frame $\mathcal{E}$ with the axial position z_{mov} and the angular position φ_{mov}. **(b)** Open loop block diagram for the linear/axial z-dynamics with input disturbance F_{load}. **(c)** Open loop block diagram for the rotary/angular φ-dynamics with input disturbance M_{cogg}.

A. LINEAR/AXIAL POSITION DYNAMICS

In order to describe its axial z-motion, the piston of the *ShuttlePump* is modeled as a rigid body with mass m_{mov} (cf. **Fig. 6 (a)**), for which the force balance

$$\frac{\mathrm{d}^2 z}{\mathrm{d}t^2} = \frac{1}{m_{\mathrm{mov}}} F_{\mathrm{tot}} = \frac{1}{m_{\mathrm{mov}}} \left(F_z + F_{\mathrm{cogg}} - F_{\mathrm{fric}} - F_{\mathrm{load}}\right) \tag{2}$$

is written. In detail:

- F_z is the electro-mechanical internal axial force generated and exerted by the stator of the LA on the mover. It is the input of the system.
- F_{cogg} is the cogging force of the LA. Due to its small amplitude (by design, [16]), it can be neglected and eventually modeled as an input disturbance.
- F_{fric} is the friction force, modeled as a viscous friction $F_{\mathrm{fric}} = b_{\mathrm{lin}} \frac{\mathrm{d}z}{\mathrm{d}t}$ with the coefficient b_{lin} representing the viscosity of blood.
- F_{load} is the required hydrodynamic load force of **Fig. 5 (a)**. Although this actually depends on the axial position z_{mov}, it is not included in the plant, but modeled as an external input disturbance.

The equilibrium points of the dynamics in (2) are found imposing $\frac{\mathrm{d}^2 z}{\mathrm{d}t^2} = 0$. This is satisfied for $z = z_{\mathrm{ss}} = \mathrm{const}$, with $z_{\mathrm{ss}} \in [-z_{\mathrm{strk}}, z_{\mathrm{strk}}]$, and with the steady-state input force $F_{\mathrm{z,ss}} = F_{\mathrm{load}}$. The plant in the Laplace domain becomes

$$G_{\mathrm{z}}(s) = \frac{Z_{(\mathrm{s})}}{F_{\mathrm{z}}(s)} = \frac{1}{m_{\mathrm{mov}}\, s^2 + b_{\mathrm{lin}}\, s}, \tag{3}$$

which is valid $\forall z_{\mathrm{ss}} \in [-z_{\mathrm{strk}}, z_{\mathrm{strk}}]$. G_{z} has one pole in the origin ($\lambda_{\mathrm{z},1} = 0$) and one pole in the left-half plane ($\lambda_{\mathrm{z},2} = -b_{\mathrm{lin}}/m_{\mathrm{mov}}$), so it is only *marginally stable* in open loop. The modeled plant for the axial dynamics is finally represented by the block diagram in **Fig. 6 (b)**.

B. ROTARY/ANGULAR POSITION DYNAMICS

For what concerns the rotational φ-dynamics, the piston is analogously modeled as a rigid body with a moment of inertia

J_{mov} and the torque balance

$$\frac{\mathrm{d}^2\varphi}{\mathrm{d}t^2} = \frac{1}{J_{\mathrm{mov}}} M_{\mathrm{tot}} = \frac{1}{J_{\mathrm{mov}}} \left(M_{\mathrm{ax}} + M_{\mathrm{cogg}} - M_{\mathrm{fric}} - M_{\mathrm{load}}\right) \tag{4}$$

is written. Similarly:

- M_{ax} is the electro-mechanical internal torque generated and applied by the RA to the mover. It is the input of the system.
- M_{cogg} is the cogging force of the RA, reported in **Fig. 5 (b)**. Also in this case, although it exhibits a dependency on the rotary position φ_{mov}, it is modeled as an external input disturbance to the system.
- $M_{\mathrm{fric}} = b_{\mathrm{rot}} \frac{\mathrm{d}\varphi}{\mathrm{d}t}$ is the viscous friction torque, modeled with the coefficient b_{rot} representing the blood viscosity for the rotary motion.
- M_{load} is the required hydrodynamic load torque.

The equilibrium points of (4) are found for $\frac{\mathrm{d}^2\varphi}{\mathrm{d}t^2} = 0$, which is satisfied for $\varphi = \varphi_{\mathrm{ss}} = \mathrm{const}$, with $\varphi_{\mathrm{ss}} \in [0, 2\pi]$, and with the steady-state input torque $M_{\mathrm{ax,ss}} = -M_{\mathrm{cogg}} + M_{\mathrm{load}}$. The plant in the Laplace domain becomes

$$G_{\varphi}(s) = \frac{\Phi_{(\mathrm{s})}}{M_{\mathrm{ax}}(s)} = \frac{1}{J_{\mathrm{mov}}\, s^2 + b_{\mathrm{rot}}\, s}. \tag{5}$$

Analogously to (3), this has the poles $\lambda_{\varphi,1} = 0$ and $\lambda_{\mathrm{z},2} = -b_{\mathrm{rot}}/J_{\mathrm{mov}}$. The modeled plant for the rotary dynamics is represented by the block diagram in **Fig. 6 (c)**.

C. ELECTRICAL DYNAMICS IN THE MOVER-ORIENTED FRAME

The dynamic model of the electrical subsystem describes the transient behavior of each phase current of the LiRA. As known, this is captured by the stator equation, which can be written for both the LA or the RA by simple analysis of the equivalent circuit model of **Fig. 7 (a)**. The stator equation is

$$\begin{aligned} u_{\mathrm{s},\{\mathrm{a,b,c}\}} &= R_{\{\mathrm{a,b,c}\}}\, i_{\mathrm{s},\{\mathrm{a,b,c}\}} + \\ &+ L_{\{\mathrm{a,b,c}\}} \frac{\mathrm{d}i_{\mathrm{s},\{\mathrm{a,b,c}\}}}{\mathrm{d}t} + u_{\mathrm{q},\{\mathrm{a,b,c}\}}, \end{aligned} \tag{6}$$

where

- $u_{\mathrm{s},\{\mathrm{a,b,c}\}}$ and $i_{\mathrm{s},\{\mathrm{a,b,c}\}}$ are the phase voltage and current, respectively,
- $R_{\{\mathrm{a,b,c}\}}$ and $L_{\{\mathrm{a,b,c}\}}$ are the phase resistance and inductance, respectively,
- $u_{\mathrm{q},\{\mathrm{a,b,c}\}} = \frac{\mathrm{d}\psi_{\{\mathrm{a,b,c}\}}}{\mathrm{d}t}$ is the induced voltage caused by the changing magnetic flux linkage with the stator coils $\psi_{\{\mathrm{a,b,c}\}}$ (reported in **Fig. 4**) due to the mover's linear and/or rotary motion.

By orienting the stator field (Field-Oriented Control) correctly with respect to the mover field, the necessary electromechanical force F_{z} or torque M_{ax} is generated. In particular, field orientation requires the electrical angle

$$\theta_{\mathrm{el}} = \begin{cases} \vartheta_{\mathrm{el}} = \frac{2\pi}{\tau_{\mathrm{pp}}}\, z_{\mathrm{mov}} & \text{for the LA} \\ \varphi_{\mathrm{el}} = P\, \varphi_{\mathrm{mov}} & \text{for the RA} \end{cases}, \tag{7}$$

where τ_{pp} is the pole pitch of the LA and P the number of pole pairs of the RA. Transforming the stator equation (6) into the mover-oriented dq-frame (cf. **Fig. 7 (c-d)**), one obtains

$$\begin{aligned} u_{\mathrm{s},\{\mathrm{d,q}\}} = R_{\{\mathrm{d,q}\}}\, i_{\mathrm{s},\{\mathrm{d,q}\}} + L_{\{\mathrm{d,q}\}} \frac{\mathrm{d}i_{\mathrm{s},\{\mathrm{d,q}\}}}{\mathrm{d}t} + \\ \underbrace{\mp \frac{\mathrm{d}\theta_{\mathrm{el}}}{\mathrm{d}t} L_{\{\mathrm{d,q}\}}\, i_{\mathrm{s},\{\mathrm{q,d}\}} + \frac{\mathrm{d}\psi_{\{\mathrm{d,q}\}}}{\mathrm{d}t} - \frac{\mathrm{d}\theta_{\mathrm{el}}}{\mathrm{d}t} \psi_{\{\mathrm{q,d}\}}}_{u_{\mathrm{ff},\{\mathrm{d,q}\}}}. \end{aligned} \tag{8}$$

As both the LA and RA have a non-salient pole translator/rotor,

$$(R_{\mathrm{d}}, L_{\mathrm{d}}) = (R_{\mathrm{q}}, L_{\mathrm{q}}) = \begin{cases} (R_{\mathrm{lin}}, L_{\mathrm{lin}}) & \text{for the LA} \\ (R_{\mathrm{rot}}, L_{\mathrm{rot}}) & \text{for the RA} \end{cases}, \tag{9}$$

whereas for the flux linkage due to field-orientation it holds

$$(\psi_{\mathrm{d}}, \psi_{\mathrm{q}}) = \begin{cases} (\hat{\Psi}_{\mathrm{PM,lin}}, 0) & \text{for the LA} \\ (\hat{\Psi}_{\mathrm{PM,rot}}, 0) & \text{for the RA} \end{cases}, \tag{10}$$

which can also be verified by transforming the phase flux linkages $\psi_{\{\mathrm{a,b,c}\}}$ in **Fig. 4** to the dq-frame. The dq-transformation of the time derivatives introduces cross-coupling terms that are compensated as feedforward voltages $u_{\mathrm{ff},\{\mathrm{d,q}\}}$. This way, the d- and q-dynamics are correctly decoupled and can hence be controlled independently. The resulting open loop plants are

$$G_{\mathrm{c},\{\mathrm{d,q}\}}(s) = \frac{1}{L_{\{\mathrm{d,q}\}}\, s + R_{\{\mathrm{d,q}\}}} \tag{11}$$

as shown in the block diagram of **Fig. 7 (b)**.

For completeness, the electrical subsystem is complemented with a simple model of the inverter used to supply the LiRA. This consists of the delay element introduced

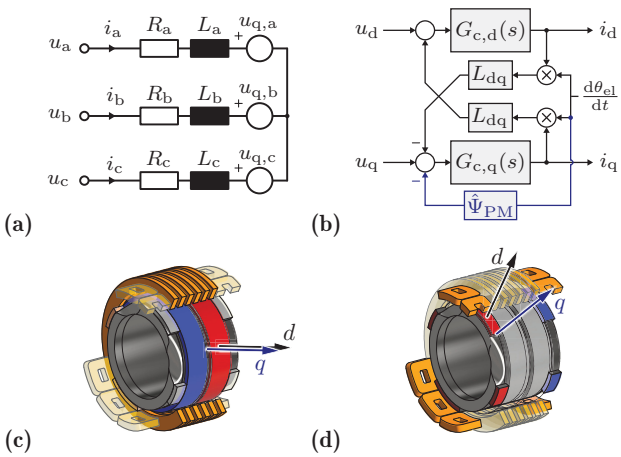

FIGURE 7. **(a)** PMSM equivalent circuit with phase resistances, inductances and induced voltages, valid either for the LA or the RA. **(b)** Open loop block diagram of the electrical subsystem in the mover-oriented frame with voltage cross-coupling terms introduced by the dq-transformation. The diagram is valid either for the LA or the RA with the generic electrical angle θ_{el} in (7). **(c)** LA part of the *ShuttlePump*, with indicated mover-oriented frame. **(d)** RA part of the *ShuttlePump*, with indicated mover-oriented frame.

by the power electronics and the foreseen LC output filter (cf. **Sec. V**). For the former, a first order approximation is sufficient, i.e.,

$$G_{\mathrm{PE}}(s) = \frac{1}{T_{\mathrm{PE}}\, s + 1}, \tag{12}$$

where T_{PE} is the sum of the switching period and the controller update period. For the latter, the transfer function has the well-known second-order form

$$G_{\mathrm{LC}}(s) = \frac{1}{L_{\mathrm{f}} C_{\mathrm{f}}\, s^2 + \frac{L_f}{R_f}\, s + 1}, \tag{13}$$

where L_f and C_f are the filter capacitance and inductance and R_f is the resistance of the damping resistor.

IV. CONTROL SYSTEM DESIGN

This section covers the design of the linear-rotary position control system of the *ShuttlePump* LiRA.

A. CONTROL STRUCTURE AND SPECIFICATIONS

Position or speed control of PMSMs typically makes use of the well-established technique of cascaded control. As the mechanical linear and rotary dynamics are well decoupled, they are controlled by independent single-input-single-output (SISO) controllers. Therefore, as illustrated in the diagram of **Fig. 8**, there is two independent cascaded controllers, each consisting of an outer control loop for the (slower) mechanical linear or rotary dynamics and an inner control loop for the (faster) electrical dynamics. For these to work properly, it is necessary to guarantee that the dynamics of the two loops are decoupled. Specifically, the inner electrical loop is expected to regulate the required force- or torque-generating current components 'almost instantly' from the point of view of the outer mechanical loop. In the frequency domain, this means that the closed-loop bandwidth of the inner loop should be much larger (e.g., by a factor 10) than the one of outer loop. This leads to the definition of the control specifications in **Tab. 3**. The motion control requirements previously defined in **Sec. II-C** are complemented with frequency-domain specifications on the control bandwidths and the input saturation limits. As all the controllers need to be implemented digitally, the design is first conducted in continuous time and the discretization is performed in a second step.

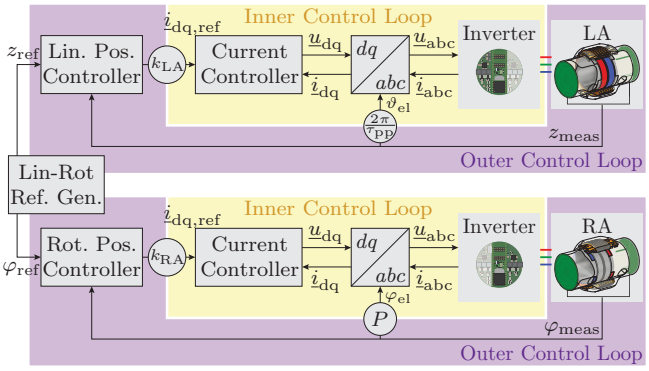

FIGURE 8. Overall control diagram of the *ShuttlePump* LiRA. The two independent cascaded loops consist of an outer linear or rotary position control loop and an inner dq-current control loop. The two loops get synchronized linear and rotary position references from the reference generator.

TABLE 3. LiRA control specifications for the *ShuttlePump*.

	LA dq-Current	RA dq-Current
Max tracking error	$i_{\{\mathrm{d,q}\},\mathrm{err}} = 0.05\,\mathrm{A}$	$i_{\{\mathrm{d,q}\},\mathrm{err}} = 0.05\,\mathrm{A}$
Control BW	$\omega_{\mathrm{c}} = 2\pi\,600\,\mathrm{rad\,s^{-1}}$	$\omega_{\mathrm{c}} = 2\pi\,600\,\mathrm{rad\,s^{-1}}$
Input sat. limit	$u_{\{\mathrm{d,q}\},\mathrm{lim}} = \pm 13\,\mathrm{V}$	$u_{\{\mathrm{d,q}\},\mathrm{lim}} = \pm 13\,\mathrm{V}$
	Linear Position z	Rotary Position φ
Max tracking error	$z_{\mathrm{err,max}} = 1\,\mathrm{mm}$	$\varphi_{\mathrm{err,max}} = 5^\circ$
Control BW	$\omega_z = 2\pi\,150\,\mathrm{rad\,s^{-1}}$	$\omega_\varphi = 2\pi\,80\,\mathrm{rad\,s^{-1}}$
Input sat. limit	$F_{\mathrm{lim}} = \pm\, k_{\mathrm{LA}}\, 2.7\,\mathrm{A}$	$M_{\mathrm{lim}} = \pm\, k_{\mathrm{RA}}\, 0.5\,\mathrm{A}$

B. CURRENT CONTROLLER DESIGN

For the dq-current controllers, a simple PI controller of the type

$$K_{\mathrm{PI,c}}(s) = k_{\mathrm{p,c}} + k_{\mathrm{i,c}}\, \frac{1}{s} \tag{14}$$

is sufficient, implemented as in **Fig. 9 (a)**. This can, e.g., be tuned with classical *loop shaping* methods [23]. The electrical plant considered is $G_{\mathrm{c,tot}}(s) \approx G_{\mathrm{c}}(s)$, i.e., the influence of the LC output filter and of the delays introduced by the power electronics are neglected. This is allowed, as for frequencies up to the targeted $\omega_{\mathrm{c}} = 2\pi\,600\,\mathrm{rad\,s^{-1}}$, $G_{\mathrm{LC}}(s)$ and $G_{\mathrm{PE}}(s)$ are both approximately equal to 1. As shown in the bode diagram of **Fig. 9 (b)**, the crossover frequency of the loop gain $L_{\mathrm{c}}(s) = G_{\mathrm{c}}(s)\, K_{\mathrm{PI,c}}(s)$ is set to the desired closed-loop bandwidth $\omega_{\mathrm{c}} = 2\pi\,600\,\mathrm{rad\,s^{-1}}$. This correctly reflects in the complementary sensitivity $T_{\mathrm{c}}(s) = L_{\mathrm{c}}(s)/(1 + L_{\mathrm{c}}(s))$. The specified phase margin is $\phi_{\mathrm{c}} = 50^\circ$ to guarantee a fast response, even at the cost of a slightly underdamped behavior, that is nevertheless tolerable by the system. The necessary PI gains for this design are reported in **Tab. 4**, both for the LA and the RA case.

The designed controller $K_{\mathrm{PI,c}}(s)$ is tested in simulation on an accurate model of the LiRA built in the software PLECS [22]. The results of the simulation are reported in **Fig. 9 (c)**. The assigned references are representative of typical operation: for the q-current a sine with amplitude $i_{\mathrm{q,nom}} = 2\,\mathrm{A}$ and frequency $f_{\mathrm{op,max}} = 5\,\mathrm{Hz}$, whereas for the d-current a constant $i_{\mathrm{d,ref}} = 0\,\mathrm{A}$. Note that while the q-current is correctly tracked, the d-current is not disturbed and successfully kept to 0 A due to proper decoupling of the two current components. Furthermore, it can be seen that the q-voltage stays within the saturation limits $u_{\{\mathrm{d,q}\},\mathrm{lim}} = \pm 13\,\mathrm{V}$. To account for eventual voltage saturations, the integrator of the PI controller is implemented with an anti-windup scheme, using conditional integration [24].

C. LINEAR/AXIAL POSITION CONTROLLER DESIGN

For the z-position controller, derivative action is also needed to reach the targeted closed-loop bandwidth ω_{z} without

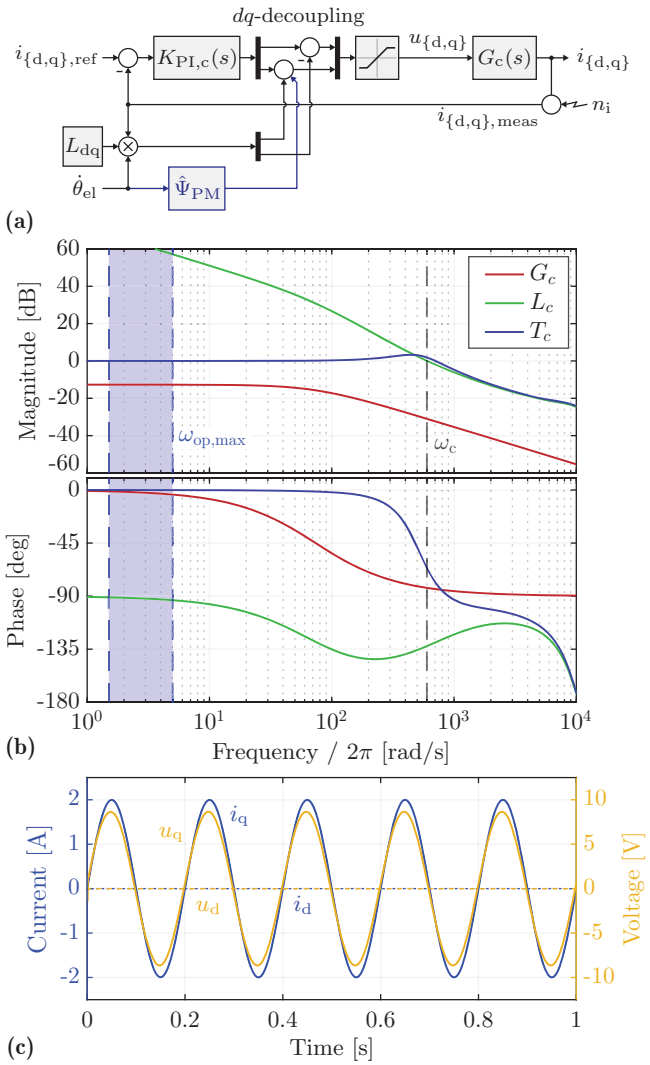

FIGURE 9. **(a)** Closed-loop dq-current control block diagram, valid either for the LA or the RA electrical subsystems in the mover-oriented frame. The d- and q-voltages commanded by the PI controller $K_{\mathrm{PI,c}}(s)$ are corrected with feed-forward components for proper decoupling of the d- and q- dynamics (cf. **Fig. 7 (b)**). **(b)** Bode plots of the current control loop (LA case): plant $G_c(s)$, loop gain $L_c(s)$ and complementary sensitivity $T_c(s)$. **(c)** Simulated tracking response (PLECS [22], LA case) for the references $i_{\mathrm{q,ref}} = 2\,\mathrm{A}\sin(2\pi\,5\,t)$ and $i_{\mathrm{d,ref}} = 0$, together with voltage commands $u_{\{\mathrm{d,q}\}}$.

prohibitively large gains. The PID controller is typically implemented in the form

$$K_{\mathrm{PID,z}}(s) = k_{\mathrm{p,z}} + k_{\mathrm{i,z}}\,\frac{1}{s} + k_{\mathrm{d,z}}\,\frac{s}{\frac{1}{k_{\mathrm{f,z}}}\,s + 1}, \qquad (15)$$

i.e., with a first-order filter on the derivative term. This makes the derivative term proper and hence practically realizable. Furthermore, it beneficially reduces high-frequency noise introduced, e.g., by the measurement signals. Another option is to implement a *state observer*, which provides a smooth estimate of the axial translational speed $\dot{z}_{\mathrm{est}}$ to be used for the derivative action. Note that the dot notation $\dot{(\star)}$ is used to indicate the time-derivative $\mathrm{d}(\star)/\mathrm{d}t$. The state observer can also provide a smooth estimate of the axial position z_{est}, which is used for control as well. As shown in the block

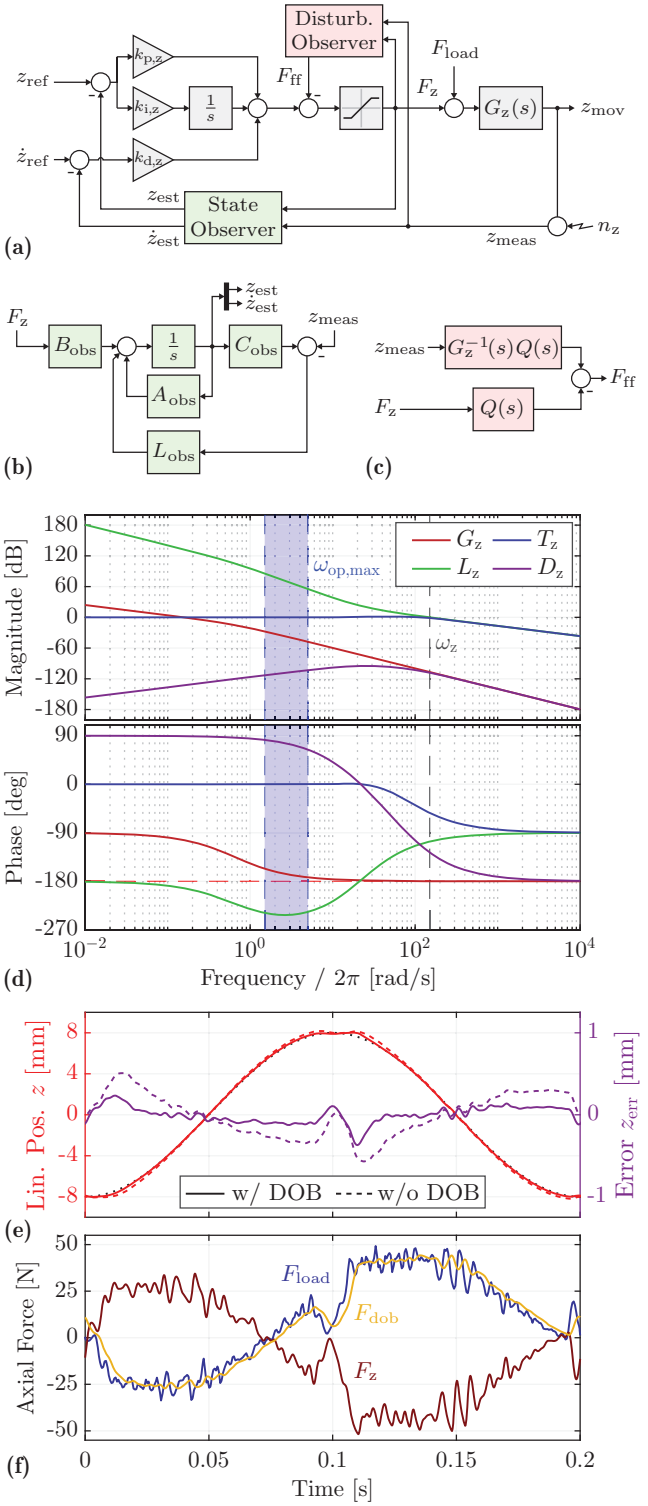

FIGURE 10. **(a)** Closed-loop z-position control block diagram, employing a state observer and a disturbance observer. **(b)** Implemented Luemberger observer, estimating the linear position z_{mov} and speed $\dot{z}_{\mathrm{mov}}$ from the measured position z_{meas} and the force command F_{z}. **(c)** Implementation of the disturbance observer with the filter $Q(s)$ to perform the plant inversion of $G_{\mathrm{z}}(s)$. **(d)** Bode plots of the linear position control loop: plant $G_{\mathrm{z}}(s)$, loop gain $L_{\mathrm{z}}(s)$, complementary sensitivity $T_{\mathrm{z}}(s)$, and disturbance transfer $D_{\mathrm{z}}(s)$. **(e)** Simulated reference tracking (PLECS): response and tracking error with (solid line) and without (dashed line) disturbance observer feedforwarded. **(f)** Simulated reference tracking (PLECS): corresponding load/disturbance force F_{load}, force command F_{z}, and observed force F_{dob}.

diagram of **Fig. 10 (a)**, the control action (or force command) is then computed as

$$F_z = k_{\mathrm{p,z}}(z_{\mathrm{ref}} - z_{\mathrm{est}}) + k_{\mathrm{i,z}} \int (z_{\mathrm{ref}} - z_{\mathrm{est}})\,\mathrm{d}t + k_{\mathrm{d,z}}\,(\dot{z}_{\mathrm{ref}} - \dot{z}_{\mathrm{est}}), \tag{16}$$

where z_{ref} is the reference position and $\dot{z}_{\mathrm{ref}}$ its time-derivative (that can be, e.g., pre-computed). The chosen state observer is a Luenberger observer, shown in the diagram of **Fig. 10 (b)** [25], [26]. In order to use the estimates z_{est} and $\dot{z}_{\mathrm{est}}$ for closed-loop control, they have to converge to the estimated values reasonably fast with respect to the targeted bandwidth of the z-controller ω_{z}. Therefore, the poles of the observer should be placed on the left-half plane with a real (negative) part equal to or greater than about $5 \cdot \omega_{\mathrm{z}}$.

The targeted control bandwidth $\omega_{\mathrm{z}} = 2\pi\,150\,\mathrm{rad\,s^{-1}}$ is chosen to provide good reference tracking up to $\omega_{\mathrm{z,ref}} = 2\pi\,5\,\mathrm{rad\,s^{-1}}$ (recall that the maximum operational frequency of the *ShuttlePump* is 5 Hz). For this purpose, $\omega_{\mathrm{z}}/3 = 10 \cdot \omega_{\mathrm{z,ref}} = 2\pi\,50\,\mathrm{rad\,s^{-1}}$ would already be sufficient. However, it is necessary to consider also the load force F_{load}, acting as a heavy input disturbance to the system. As visible from **Fig. 5 (a)**, this has a fundamental component with frequency $\omega_{\mathrm{z,dist}} = \omega_{\mathrm{z,ref}}$ (i.e., the same as the reference), but a rather large amplitude $\tilde{F}_{\mathrm{load}} = 33\,\mathrm{N}$. The larger the control bandwidth, the better the disturbance due to F_{load} is rejected. This can be seen by considering the disturbance transfer

$$D_{\mathrm{z}}(s) = \frac{G_{\mathrm{z}}(s)}{1 + G_{\mathrm{z}}(s)\,K_{\mathrm{PID,z}}(s)}, \tag{17}$$

which can be used to study the disturbance rejection capabilities of the control loop. As visible in the Bode plot of **Fig. 10 (d)**, the magnitude of $D_{\mathrm{z}}(s)$ exhibits a positive $20\,\mathrm{dB/dec}$ slope for frequencies below about $0.1 \cdot \omega_{\mathrm{z}}$. The shown Bode plots correspond to a PID z-controller tuned with $\omega_{\mathrm{z}} = 2\pi\,150\,\mathrm{rad\,s^{-1}}$ and a phase margin $\phi_{\mathrm{z}} = 30°$ using the `pidtune` command in MATLAB, with the gains indicated in **Tab. 4**. Assuming the load force consists solely of its fundamental component, i.e., $F_{\mathrm{load}} = \tilde{F}_{\mathrm{load}} \sin(2\pi\,\omega_{\mathrm{z,dist}})$, the disturbance response would have an amplitude $z_{\mathrm{dist}} = |D_{\mathrm{z}}(j\,\omega_{\mathrm{z,ref}})| \cdot \tilde{F}_{\mathrm{load}} = 0.21\,\mathrm{mm}$, which is adequately small.

The disturbance rejection can be further enhanced with a feed-forward component F_{ff} on the force command that compensates F_{load}. One option is to preprogram $F_{\mathrm{ff}} \approx F_{\mathrm{load}}$ according to, e.g., the results of the CFD simulations. Ideally, if F_{load} was perfectly predicted, it could be completely compensated. Nevertheless, this is hardly the case due to the nature of the hydrodynamic forces acting on the piston. If F_{ff} is substantially incorrect, it could lead to even worse reference tracking results compared to the case when it is not added at all. This can happen under certain circumstances and operating conditions, like, e.g., for a reduced/increased head pressure, and hence load force. A more advanced option is to implement a *disturbance observer* (DOB) [27]–[29]. Similarly to the state observer, this exploits the model of the plant $G_{\mathrm{z}}(s)$ to calculate an estimate F_{dob} of the load force F_{load}. The disturbance observer is implemented as in **Fig. 10 (c)**. In order to invert the plant $G_{\mathrm{z}}(s)$, it is necessary to introduce a filter term

$$Q(s) = \left(\frac{\omega_{\mathrm{dob}}}{s + \omega_{\mathrm{dob}}}\right)^q \tag{18}$$

with order q, chosen such that $G_{\mathrm{z}}^{-1}(s)\,Q(s)$ is proper. For the case at hand, $q = 2$. The cutoff frequency ω_{dob} should be on one hand large enough to provide good tracking of the disturbance F_{load}, but, on the other hand, not too large to avoid introducing noise in the feedback loop. In the case at hand, $\omega_{\mathrm{dob}} = 2\pi\,100\,\mathrm{rad\,s^{-1}}$ is selected.

The controller is tested in the PLECS model and the simulation results are shown in **Fig. 10 (e)** and **(f)**. To better visualize the details, only one period of the 5 Hz operation is shown. **Fig. 10 (e)** shows successful tracking of the sinusoidal reference with amplitude $z_{\mathrm{strk}} = 8\,\mathrm{mm}$, and the corresponding tracking error z_{err}. Two cases are simulated, namely with and without disturbance observer used as feed-forward compensation. Without disturbance observer, z_{err} is already below the specified boundaries, with a maximum absolute error $z_{\mathrm{err,max}} = \max(|z_{\mathrm{err}}|) = 0.57\,\mathrm{mm}$. The disturbance observer helps reduce the tracking error to an absolute maximum of $z_{\mathrm{err,max}} = 0.37\,\mathrm{mm}$. The corresponding force command F_{z} is reported in **Fig. 10 (f)**, and it is compared to the disturbance load force F_{load}. To effectively compensate it, the force F_{dob} estimated by the disturbance observer, which closely captures F_{load}, is subtracted from the force command F_{z}.

D. ROTARY/ANGULAR POSITION CONTROLLER DESIGN

For the φ-position controller, it is possible to follow analogous design considerations as for the presented z-position controller. The block diagram of the control loop is shown in **Fig. 11 (a)**. Also in this case a derivative term is needed and provided by a Luenberger state observer for the rotary dynamics, in the same form seen in **Fig. 10 (b)**. The targeted bandwidth is $\omega_{\varphi} = 2\pi\,80\,\mathrm{rad\,s^{-1}}$, chosen to track the ramp reference φ_{ref} with a slope of $2\pi\,5\,\mathrm{rad\,s^{-1}}$. The controller is again tuned with the aid of the `pidtune` command in MATLAB, the selected phase margin is $\phi_{\varphi} = 40°$ and the necessary gains can be found in **Tab. 4**. The corresponding Bode plots are shown in **Fig. 11 (b)**. This time, the main disturbance to the system is the cogging torque M_{cogg}. Its effect is not as severe as the load force disturbing the z-controller. Therefore, with the chosen bandwidth, M_{cogg} is already largely attenuated, and no special disturbance rejection measure is taken. Optionally, it would be possible to introduce a preprogrammed feed-forward torque component $M_{\mathrm{ff}} \approx M_{\mathrm{cogg}}$ [30], [31]. In fact, the profile of the cogging torque is well-known from the Finite Element Methods simulations of the RA (more accurately than what CFD simulations would predict for F_{load}).

The results of a PLECS simulation are shown in **Fig. 11 (c)** and **(d)**. As expected from the *system type* of the loop

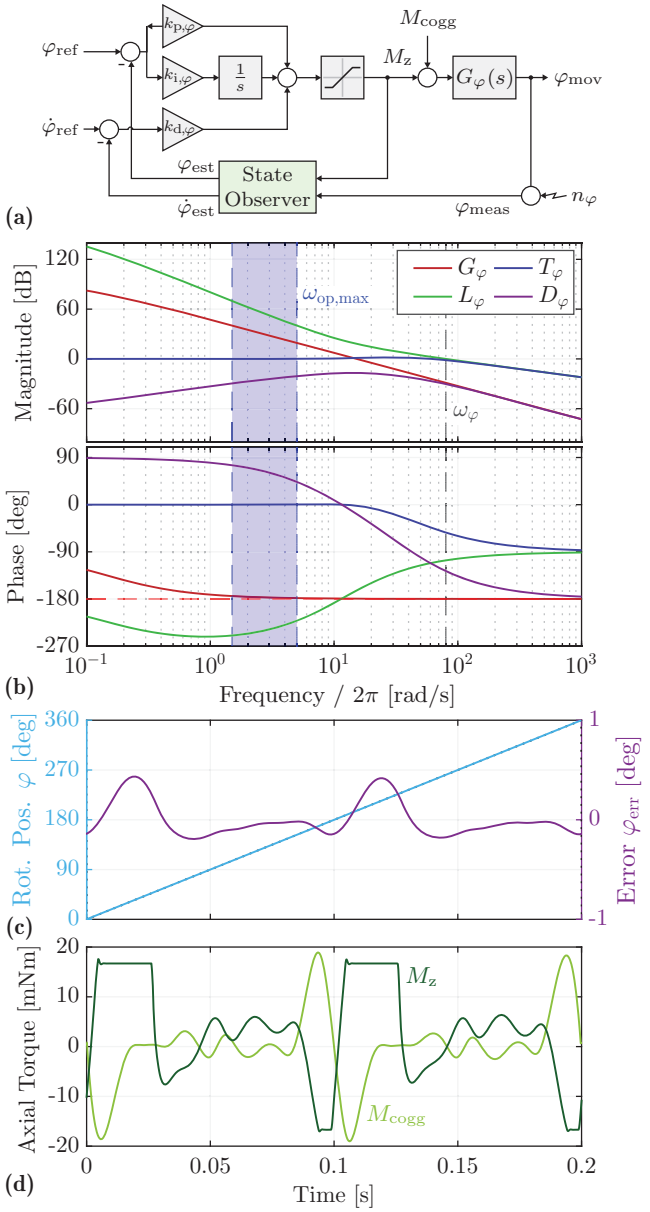

FIGURE 11. **(a)** Closed-loop φ-position control block diagram, employing a state observer. **(b)** Bode plots of the rotary position control loop: plant $G_\varphi(s)$, loop gain $L_\varphi(s)$, complementary sensitivity $T_\varphi(s)$, and disturbance transfer $D_\varphi(s)$. **(c)** Simulated reference tracking (PLECS): response and tracking error. **(d)** Simulated reference tracking (PLECS): corresponding cogging/disturbance torque M_{cogg} and torque command M_z.

gain (that contains one integrator), the ramp reference φ_{ref} can be tracked very tightly (ideally with zero steady-state error). The tracking error φ_{err} in $Fig.\ 11\ (c)$, not larger than $\varphi_{\text{err,max}} = \max(|\varphi_{\text{err}}|) = 0.57°$, is then caused by the disturbance M_{cogg}. In particular, **Fig. 11 (d)** shows how the torque command M_{z} counters the cogging torque M_{cogg}, but reaches its saturation limits. During the intervals while the control action is saturated, the tracking error is the largest. Nevertheless, this is not of concern, as φ_{err} is way within the specified boundaries (cf. **Tab. 3**).

TABLE 4. Chosen controller gains/parameters and execution frequencies

	Linear Position z		Rotary Position φ	
k_{p}	$6.18 \cdot 10^4$	N m^{-1}	7.80	N m rad^{-1}
k_{i}	$4.24 \cdot 10^6$	$\text{N m}^{-1}\,\text{s}^{-1}$	$2.83 \cdot 10^2$	$\text{N m rad}^{-1}\,\text{s}^{-1}$
k_{d}	$2.25 \cdot 10^2$	N s m^{-1}	$5.37 \cdot 10^{-2}$	N m s rad^{-1}
l_{11}	$9.89 \cdot 10^3$	s^{-1}	$5.28 \cdot 10^3$	s^{-1}
l_{12}	$2.44 \cdot 10^7$	s^{-2}	$6.94 \cdot 10^6$	s^{-2}
f_{ex}	10	kHz	10	kHz
	LA dq-Current		RA dq-Current	
k_{p}	$2.41 \cdot 10^1$	V A^{-1}	$3.16 \cdot 10^1$	V A^{-1}
k_{i}	$9.76 \cdot 10^4$	$\text{V A}^{-1}\,\text{s}^{-1}$	$1.63 \cdot 10^5$	$\text{V A}^{-1}\,\text{s}^{-1}$
f_{ex}	20	kHz	20	kHz

E. CONTROLLER DISCRETIZATION

Once the design in continuous time is completed, the controllers need to be discretized for digital implementation. The execution frequency (or reciprocally time) of each controller $f_{\text{ex}} = 1/T_{\text{ex}}$ is indicated in **Tab. 4**. Given that the execution frequencies are much larger than the chosen control bandwidths, the mapping used is the *Forward-Euler*, for which the gains are adapted as $k_{\text{p,disc}} = k_{\text{p,cont}}$, $k_{\text{i,disc}} = k_{\text{i,cont}} \cdot T_{\text{ex}}$, and $k_{\text{d,disc}} = k_{\text{d,cont}} \cdot f_{\text{ex}}$.

V. HARDWARE IMPLEMENTATION

This section presents the hardware PCB prototype of the inverter and control unit on which the designed and discretized controller is implemented. Furthermore, the experimental assembly of the LiRA and the custom test bench used for measurements are described.

A. INVERTER AND CONTROL UNIT

The six-phase inverter unit and the digital control unit are implemented together on a single, compact PCB (Ø 54 mm), shown in **Fig. 12 (b)**. The inverter unit consists of two identical parts, each based on the *MP6536* integrated inverter module from *Monolitic Power Systems*. This is selected as it conveniently offers a three-phase inverter of adequate power level together with integrated gate drivers in a single 5-by-5 mm chip. The IC can be operated with a DC-link voltage up to $U_{\text{DC,max}} = 26\,\text{V}$, which is the finally selected value U_{DC}. The maximum phase current is 5 A and the on-state resistance of the power MOSFETS is $R_{\text{ds,on}} = 240\,\text{m}\Omega$. For the first animal tests, the inverter and control unit will be extracorporeal. Therefore, as illustrated by **Fig. 12 (a)**, a long (approx. 2 m) percutaneous driveline is needed to realize the connection with the implanted *ShuttlePump*. In order to prevent signal reflections along the driveline and unwanted disturbances to the sensors due to the inverter's switching frequency, it is necessary to utilize LC filters at the output of the inverter modules. The value of the filter inductor L_{f} is selected together with the switching frequency f_{sw} to guarantee a certain worst-case peak-to-peak inductor current ripple

$$\Delta i_{\text{L}_\text{f},\text{max}} = \frac{U_{\text{DC}}}{4\, f_{\text{sw}}\, L_f} < 0.3\,\text{A}. \tag{19}$$

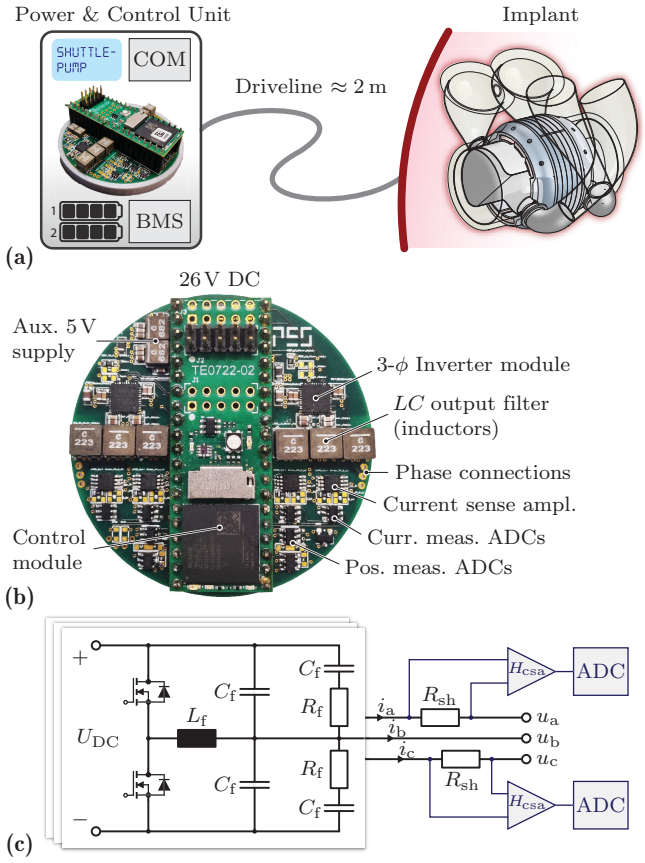

FIGURE 12. **(a)** Overall *ShuttlePump* TAH system. The power and control unit hosting the inverter, the battery pack and the communication interface is connected to the implanted pump via a percutaneous driveline. **(b)** Realized inverter board and its components. The diameter of the PCB is 54 mm. **(c)** Circuit schematic of one phase of the three-phase inverter with LC output filter and in-line current measurements with shunt resistors on two phases.

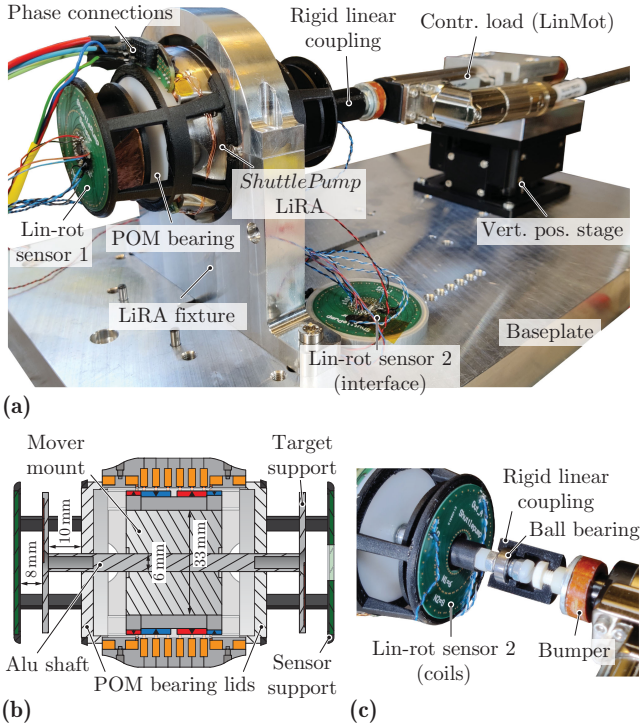

FIGURE 13. **(a)** Experimental test bench used to commission the linear-rotary position controller of the *ShuttlePump* LiRA. This is coupled with a custom linear coupling to a linear motor (*LinMot* [32]), used as a controllable axial load. **(b)** Cross-sectional view of the *ShuttlePump* LiRA with a simplified mechanical bearing system. The mover is fixed to an aluminum shaft, which is held by two side bearing lids made of POM. **(c)** Replacement version of the sensor with a 12 mm hole, to allow coupling the mover of the *ShuttlePump* to the controllable axial load. The realized custom linear coupling integrates a rotary ball bearing.

As the inductor volume scales with L_f, for a compact realization the highest possible f_{sw} is used, which for the *MP6536* is $f_{sw} = 1\,\text{MHz}$. The needed inductance is then $L_f = 22\,\mu\text{H}$. The cutoff frequency of the LC filter is accordingly placed two decades lower, i.e., $f_{LC} = 10^{-2} \cdot f_{sw} = 10\,\text{kHz}$, by using $C_f = 10\,\mu\text{F}$. The damping resistor is $R_f = 2\,\Omega$. For current control, two in-line phase current measurements per module are used. These are based on the voltage drop u_{sh} over a $R_{sh} = 30\,\text{m}\Omega$ shunt resistor, which is then amplified by a current sense amplifier with gain $H_{csa} = 20\,\text{V/V}$ (*MAX40056TAUA+*). The amplified voltage is sampled by an ADC with 10 bits and 5 V analog input range, giving a current measurement resolution

$$i_{res} = \frac{1}{R_{sh}\,H_{csa}}\,\frac{5\,\text{V}}{2^{10}} = 8.1\,\text{mA}. \tag{20}$$

The same ADCs are also used for the position sensor signals and are placed on the bottom part of the board. Finally, the core of the control unit is the *TE-0722* module by *Trenz Electronic*, with the *AMD/Xilinx Zynq 7010* system on chip. The current and position controllers are executed by the processing unit, whereas the low-level hardware I/O interfaces (PWM modulator, ADCs, etc.) are implemented in the FPGA.

B. EXPERIMENTAL TEST BENCH

Fig. 13 (a) shows the custom experimental test bench used to verify the functionality of the designed linear-rotary position controller. On the left side of the test bench, there is the complete test assembly of the *ShuttlePump* LiRA. As visible from the sectional view of **Fig. 13 (b)**, the piston of the *ShuttlePump* is replaced with a simplified structure holding together the mover of the LiRA and the semi-circular copper sensor targets through an aluminum shaft. At each side of the stator of the LiRA, there is a round lid made of POM with a center hole, through which the aluminum shaft can be inserted and slid with low friction. This way, the mover is held radially centered with respect to the stator and can still perform linear-rotary motion. This bearing system is a simplified mechanical alternative to the foreseen hydrodynamic journal bearing. In addition, the aluminum shaft facilitates the mechanical coupling of the LiRA with an external axial load. For this purpose, also a special version of the sensor is realized, with a 12 mm hole at the center of the PCB, visible in **Fig. 13 (c)**.

On the right side of the test bench, there is a linear test motor (*LinMot PS01-23x80-HP* [32]) that can be used as a

controllable axial load. The linear test motor is mounted on a vertical positioning stage to adjust its alignment with the LiRA. As the slider of the linear test motor can be freely rotated inside its stator without affecting its operation/linear force generation, it could be directly coupled to the mover of the LiRA. However, to rotate both elements and overcome the additional friction the RA would be overloaded. Therefore, a custom linear coupling is realized, which allows free rotation of the mover while transmitting the axial force generated by the linear motor. As visible from **Fig. 13 (c)** (dismounted coupling), this features a rotary ball bearing to minimize the frictional torque. The chosen driver for the test linear motor (*LinMot B1100-VF* [33]) allows force(/current) control operation with an external custom reference, which can, e.g., be programmed to emulate the realistic CFD load force profile of **Fig. 5 (a)**.

VI. EXPERIMENTAL MEASUREMENTS AND VERIFICATION

This section presents the experimental measurements demonstrating the operation of the complete LiRA system of the *ShuttlePump*, with simultaneous linear-rotary position control. The linear and rotary position signals, as well as the q-currents and q-voltages are recorded internally by the control unit after a preliminary calibration round for each quantity. In particular, the calibration of the linear position sensor is performed with the aid of the linear motor (in servo-mode).

A. LINEAR-ROTARY POSITION CONTROL: TRACKING WITH NO LOAD

The measurements for no load operation are reported in **Fig. 14**. Note that in this case the *ShuttlePump* is mechanically decoupled from the controllable load. As expected, the linear position z_{mov} tracks the specified reference z_{ref} closely (cf. **Fig. 14 (a)**), with a maximum absolute error as low as $z_{\mathrm{err,max}} = 0.38\,\mathrm{mm}$. For this case, a relatively small force F_{z} is commanded, as it can be seen from the q-current $i_{\mathrm{q,z}}$ in **Fig. 14 (b)**. The distinguishable positive and negative q-voltage and q-current peaks occur in correspondence of the linear position zero-crossings, i.e., around $z_{mov} = 0$. It should be noted that, around those instants, there is the transition from the measurement signal of one sensor to the other to calculate z_{mov} (cf. **Appendix C**). It could be observed experimentally that this transition is delicate, and introduces a slight measurement disturbance in both linear and rotary position measurements. Simultaneously, the rotary position φ_{mov} tracks its reference φ_{ref} with a maximum absolute error $\varphi_{\mathrm{err,avg}} = 4.7°$. Therefore, φ_{err} is always kept within the $\pm 5°$ error tolerance band, especially during the inlet/outlet opening/closing phases, highlighted with shaded boxes in **Fig. 14 (c)**. The torque-generating current $i_{\mathrm{q},\varphi}$ exhibits a ripple indicating that the cogging torque is being compensated. Part of this ripple is caused by the measurement disturbance introduced by the aforementioned post-processing sensor transition. The average of the current

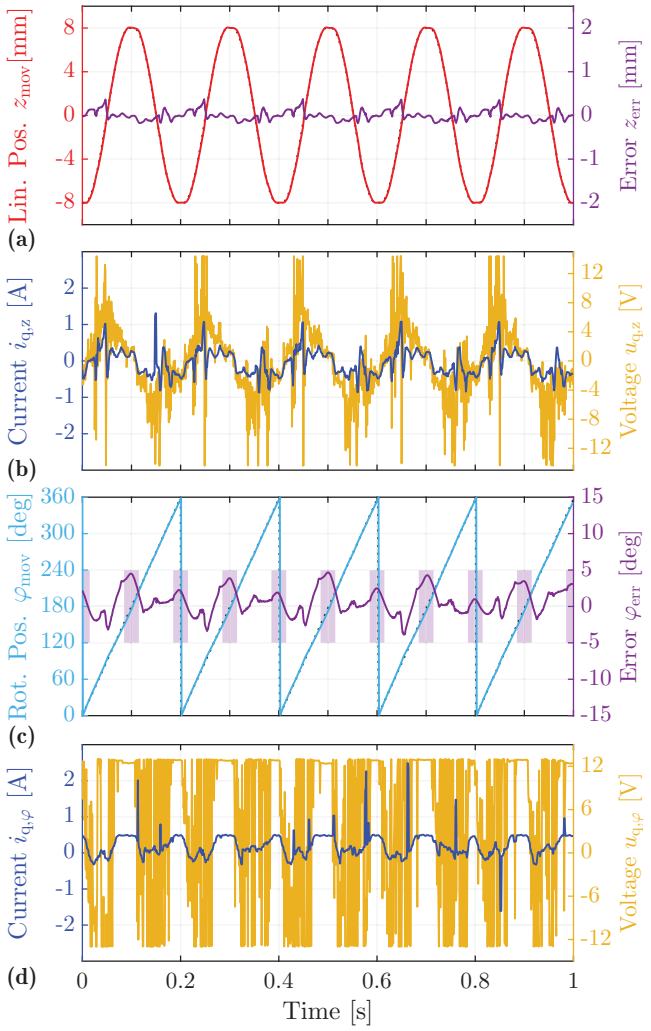

FIGURE 14. Linear-rotary position tracking measurements with no load, for $f_{\mathrm{op}} = 5\,\mathrm{Hz}$. **(a)** Linear position z_{mov} and tracking error z_{err}. **(b)** Linear q-current $i_{\mathrm{q,z}}$, with the corresponding voltage command $u_{\mathrm{q,z}}$. **(c)** Rotary position φ_{mov} and tracking error φ_{err}. The $\pm 5°$ error tolerance band during the inlet/outlet opening/closing phases is indicated with shaded boxes. **(d)** Rotary q-current $i_{\mathrm{q},\varphi}$, with the corresponding voltage command $u_{\mathrm{q},\varphi}$.

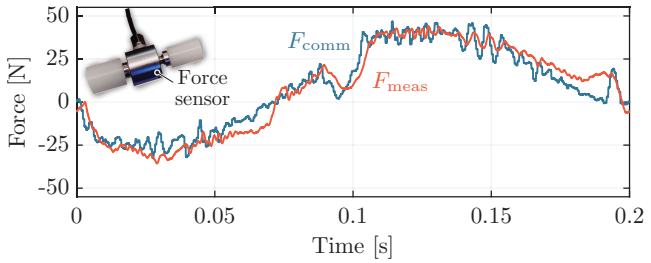

FIGURE 15. Verification of the force delivered by the controllable load. The force F_{meas}, measured by the load cell placed at coupling between the two motors, is compatible with the commanded force F_{comm}.

is $i_{\mathrm{q},\varphi,\mathrm{avg}} = 0.22\,\mathrm{A}$, which corresponds to about $7.4\,\mathrm{mN\,m}$. This is the residual friction that is still present after careful manufacturing of the contacting parts. However, in the actual application, this is substantially lower. Therefore, the fact that it is possible to keep φ_{err} within the specified boundaries

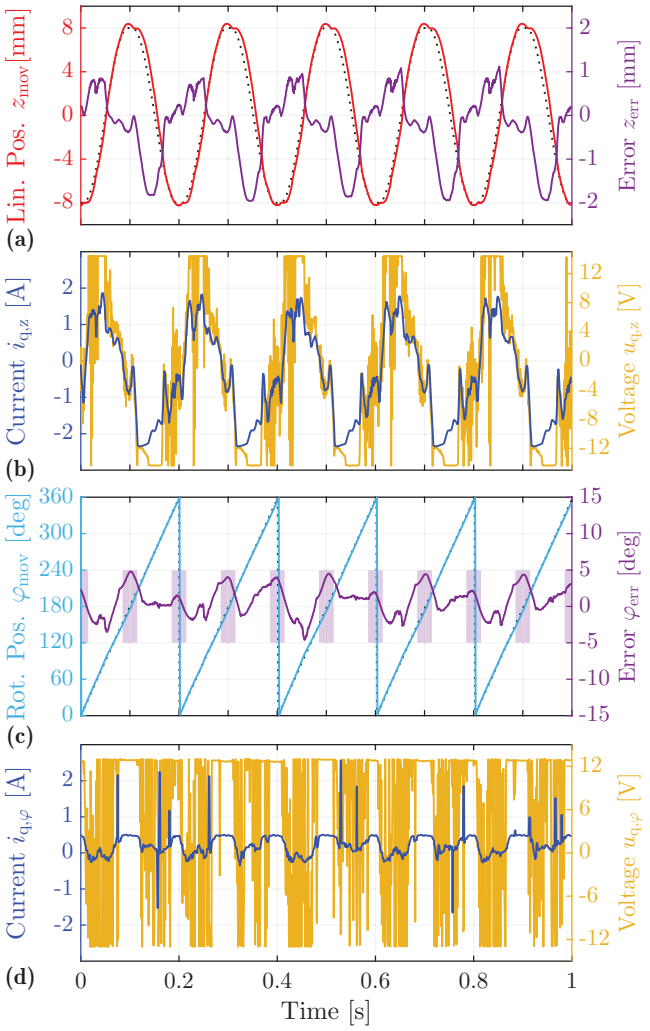

FIGURE 16. Linear-rotary position tracking measurements with full axial load and no disturbance observer in feedforward, for $f_{\mathrm{op}} = 5\,\mathrm{Hz}$. **(a)** Linear position z_{mov} and tracking error z_{err}. **(b)** Linear q-current $i_{\mathrm{q,z}}$, with the corresponding voltage command $u_{\mathrm{q,z}}$. **(c)** Rotary position φ_{mov} and tracking error φ_{err}. The $\pm 5^{\circ}$ error tolerance band during the inlet/outlet opening/closing phases is indicated with shaded boxes. **(d)** Rotary q-current $i_{\mathrm{q},\varphi}$, with the corresponding voltage command $u_{\mathrm{q},\varphi}$.

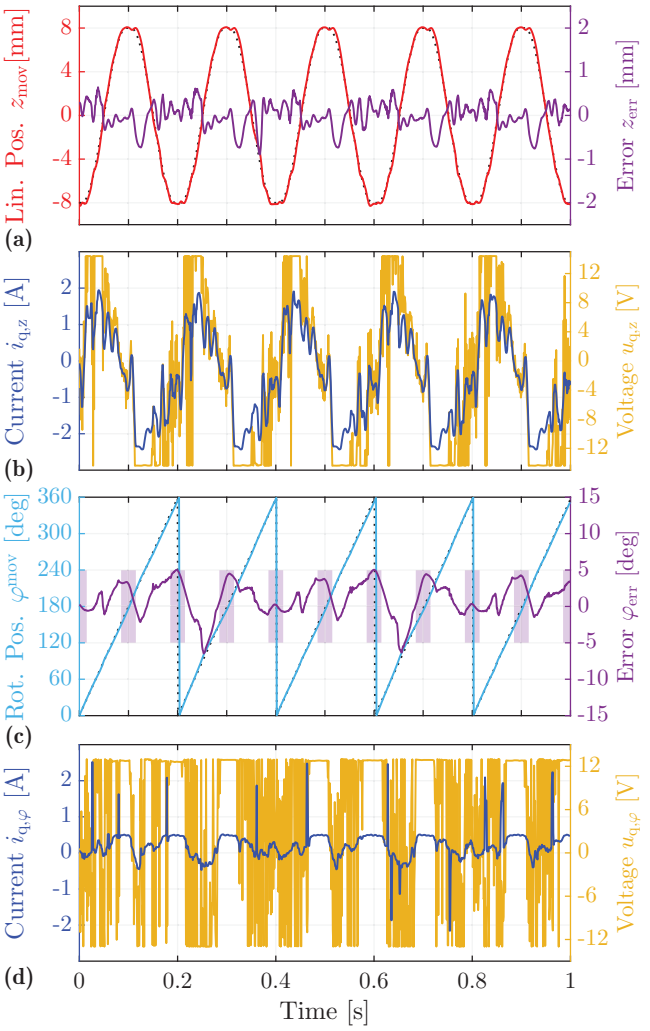

FIGURE 17. Linear-rotary position tracking measurements with full axial load and disturbance observer enabled in feedforward, for $f_{\mathrm{op}} = 5\,\mathrm{Hz}$. **(a)** Linear position z_{mov} and tracking error z_{err}. **(b)** Linear q-current $i_{\mathrm{q,z}}$, with the corresponding voltage command $u_{\mathrm{q,z}}$. **(c)** Rotary position φ_{mov} and tracking error φ_{err}. The $\pm 5^{\circ}$ error tolerance band during the inlet/outlet opening/closing phases is indicated with shaded boxes. **(d)** Rotary q-current $i_{\mathrm{q},\varphi}$, with the corresponding voltage command $u_{\mathrm{q},\varphi}$.

even for such high friction is a remarkable result.

B. LINEAR-ROTARY POSITION CONTROL: TRACKING WITH AXIAL LOAD

For this set of measurements, the *ShuttlePump* is coupled to the controllable load via the custom linear coupling (cf. **Fig. 13 (c)**). The force reference for the test motor F_{comm} is programmed to be exactly the same as the force F_{load} of **Fig. 5 (a)**, obtained from the CFD simulations. To guarantee the correct synchronization between the linear-rotary position controller commands and the controllable load, F_{comm} is sent from the inverter board to the *LinMot* driver. Before proceeding with measurements, it is verified that the force delivered by the controllable load is correct, i.e., that it tracks the reference F_{comm}. For this purpose, a force sensor is mounted at the coupling location between the *ShuttlePump* LiRA and the linear test motor. The used sensor is the miniature tension/compression load cell *Burster 8417*. Its voltage output is amplified with an instrumentation amplifier to facilitate reading on the oscilloscope. The measured force F_{meas} is compared to the force reference F_{comm} in **Fig. 15**, where it can be seen that they are in good agreement. The sensor is subsequently removed to shorten the length of the coupling between the LiRA and the test motor.

The measurements for linear-rotary position tracking with axial load are reported in **Fig. 16**. In this first case, the disturbance observer is disabled. The linear position reference is still adequately tracked under the heavy load disturbance (cf. **Fig. 16 (a)**). Clearly, this time the tracking error z_{err} is larger with respect to the no-load case, up to a maximum of $z_{\mathrm{err,max}} = 1.96\,\mathrm{mm}$. This peak, however, does not occur during the critical plateau phase. The reaction of the con-

troller countering the disturbance force is reflected in the commanded q-current $i_{\mathrm{q,z}}$, which reaches peaks around $\pm 2\,\mathrm{A}$ (cf. **Fig. 16 (b)**), corresponding to about $46\,\mathrm{N}$. The rotary position tracking is substantially unchanged, and the error φ_{err} is kept within the targeted $\pm 5°$ band.

Finally, with the disturbance observer enabled, the measurements of **Fig. 17** are obtained. The main advantage is that the maximum linear tracking error is now reduced to $z_{\mathrm{err,max}} = 0.89\,\mathrm{mm}$, and hence the $z_{\mathrm{err,max}} = 1\,\mathrm{mm}$ specification is always met. It can also be noticed that the rotary tracking error is slightly larger. Although the linear and rotary position controllers are decoupled, the linear and rotary position measurements are not. In particular, as discussed in **Appendix C**, the rotary position is obtained combining the information from the two sensors according to the measured linear position z_{meas}. The slight difference in performance is hence caused by the fact that the linear position behaves differently in the combination range for the rotary position ($z_{\mathrm{meas}} = [-2\,\mathrm{mm}, 2\,\mathrm{mm}]$, cf. **Fig. 20**). This range was initially selected to get the most satisfactory results for the case without DOB, so when this is activated and the range is not adapted, the rotary tracking error gets slightly larger. Nevertheless, it should be noticed that the worsened φ-tracking performance is limited to the range around the zero-crossings of the linear position. In the crucial intervals (i.e., for which the piston is at the two edge positions) the rotary tracking error is similar and within the specified boundaries.

VII. CONCLUSION

The operation of the blood pumps used as (left) ventricular assist devices or Total Artificial Hearts (TAHs) substantially relies on feedback control of their impeller's speed and/or position. For the novel implantable TAH *ShuttlePump*, this is especially the case due to its operating principle, which requires synchronized linear-rotary position control of its specially-shaped piston. The control system designed in this paper on a detailed electromagnetic model of the Linear-Rotary Actuator (LiRA), and subsequently implemented in a hardware demonstrator system is suitable to operate the *ShuttlePump*. The experimental results demonstrate that the specified linear-rotary motion profile can be tracked with an accuracy below $1\,\mathrm{mm}$ and $5°$ up until $5\,\mathrm{Hz}$ of operation under the heavy axial load disturbance ($45\,\mathrm{N}$ peak) introduced by the required hydraulic forces for pumping operation. The complete drive system can hence be reliably used in further experiments *in vitro* (i.e., with a dedicated hydraulic test bench) and *in vivo* (i.e., with implantation in animal models) to validate the predicted fluid-dynamic and clinical characteristics of the blood pump.

VIII. APPENDIX

This Appendix complements the paper with additional information on the realized LiRA and linear-rotary position sensors.

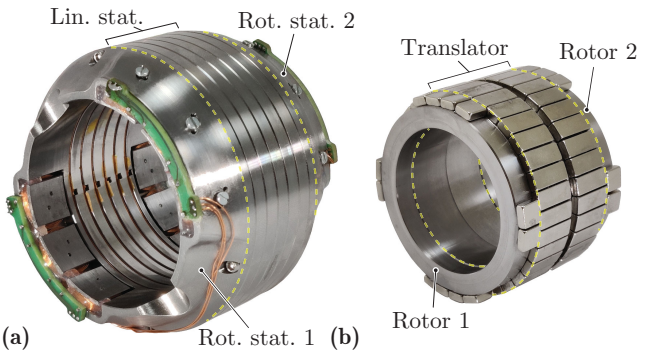

FIGURE 18. Realized hardware prototype of the LiRA of the *ShuttlePump* [16], [17]. The stator is made of *VACOFLUX50* and equipped with 6 (LA) + 12 (RA) custom-made coils. The mover is realized with NdFeB PM segments (grade N50) glued on a *VACOFLUX50* back iron. In the final pump, this is embedded in the piston and covered by a sleeve of hemocompatible material.

A. OVERVIEW OF THE REALIZED LIRA

Due to the very different mechanical output power levels, the LA and the RA are designed independently from each other, utilizing the maximum possible volume for the LA ($P_{\mathrm{mech,avg,LA}} = 3.6\,\mathrm{W}$) and then fitting the RA ($P_{\mathrm{mech,avg,RA}} = 98\,\mathrm{mW}$) in the remaining space [16], [17]. As seen in the sectional view of **Fig. 2**, both designs are based on Permanent-Magnet Synchronous Machines (PMSMs). Furthermore, the total number of phases is minimized to $N_{\mathrm{ph}} = 6$, in order to reduce the complexity of the overall drive system.

1) Linear Actuator (LA)

The LA is realized as a Tubular Linear Actuator (TLA), with $N_{\mathrm{s,LA}} = 6$ slots and $N_{\mathrm{p,LA}} = 2$ poles [16]. The stator teeth are equipped with pole shoes to minimize axial cogging forces. The poles on the mover are realized with two radially-magnetized surface-mounted permanent magnets. The TLA design is optimized with the aid of Finite Element Methods (FEM) simulations. The main design trade-off is between the ohmic losses and the radial attraction force appearing between mover and stator when the piston is off-center, which can disturb the hydrodynamic bearing. The selected TLA design is realized as a hardware prototype, visible in **Fig. 18**. It is $l_{\mathrm{stat,LA}} = 24\,\mathrm{mm}$ long and fully utilizes the volume within the maximum allowed outer diameter $d_{\mathrm{out}} = 70\,\mathrm{mm}$. Further parameters are listed in **Tab. 1**. The experimental results predict $P_{\mathrm{Cu,avg}} = 7.9\,\mathrm{W}$ of ohmic losses for continuous operation and show that the maximum radial attraction force for a $d_{\mathrm{bg}} = 140\,\mu\mathrm{m}$ displacement is $F_{\mathrm{rad}} = 23.8\,\mathrm{N}$. The measured machine constant is an important parameter for control and is hence reported in **Fig. 3 (a)**.

2) Rotary Actuator (RA)

The RA consists of two modules placed just adjacently to the two sides of the TLA [17]. Due to the tight space constraints around the enclosure of the *ShuttlePump*, the stator is split into two halves per module. All four half-stators are con-

nected in series and hence energized at the same time by only three phase currents in total. Each half-stator has $N_{\mathrm{s,RA}} = 3$ slots with a concentrated winding having one coil per phase. For the rotor, radially-magnetized PMs surface-mounted on a back iron ring are used. Due to the space constraints on the piston, they cannot cover the full circumference. It is then decided to cover four symmetrically-distributed arcs in order to prevent unwanted tilting torques on the piston during operation. Two arcs span an angle $\alpha_{\mathrm{PM}} = 45°$ and two $\alpha_{\mathrm{PM,small}} = 25°$. As the RA modules are just adjacent to the LA, the interactions between the two are important. For instance, it is necessary to equip the RA stator teeth with pole shoes with large coverage, in order to prevent unwanted axial reluctance forces when the mover is displaced from the center. Also the RA design is optimized with the aid of FEM simulations. In this case, the main trade-off to address is between ohmic losses and the pronounced torque (and hence angular speed) ripple, which is caused by the uneven distribution of PMs on the rotor. The experimental results show that the RA requires $P_{\mathrm{Cu,avg}} = 0.3\,\mathrm{W}$ of ohmic losses for continuous operation at $M_{\mathrm{ax,req}} = 3.1\,\mathrm{mN\,m}$, with a worst-case open-loop angular speed ripple of $14\,\%$ at $f_{\mathrm{op}} = 1.5\,\mathrm{Hz}$ (i.e., $\Omega_{\mathrm{op}} = 90\,\mathrm{rpm}$). The measured machine constant for the RA is reported in **Fig. 3 (b)**.

B. REALIZED LINEAR-ROTARY POSITION SENSORS

The linear-rotary position sensors of the *ShuttlePump* are presented in previous work of the authors [18]. They are realized as PCB-embedded Eddy-Current Sensors (ECSs) and are placed in front of the two sides of the piston along the axial direction, as shown in **Fig. 19 (a)**. The piston is equipped on both sides with thin $0.5\,\mathrm{mm}$ semicircular targets made of copper, on which the eddy currents are induced. This differential sensor configuration allows to improve the quality and sensitivity of the measured linear and rotary positions by appropriately combining the information from the two ECSs. In fact, when the piston is maximally distant ($\delta_{\max} = 2\,z_{\mathrm{strk}} = 16\,\mathrm{mm}$) along the axial direction from one of the ECSs, the quality of the measured signals is highly degraded for that ECS, but highly improved for the one on the opposite side. The compact multi-layer-PCB realization of **Fig. 19 (c)** hosts a circular excitation coil excited with a high frequency voltage u_{exc} at a frequency $f_{\mathrm{exc}} = 5\,\mathrm{MHz}$. The eddy currents thus circulating in the targets induce back the voltages $u_{\mathrm{pick,cos}}$ and $u_{\mathrm{pick,sin}}$ in two specially-shaped pickup coils. These are designed in such a way that the amplitudes of the two induced voltages are modulated with a sine and cosine envelope according to the angular position of the semicircular target. From the demodulated voltages, the rotary position measurements are obtained as

$$\varphi_{\{\mathrm{S1,S2}\}} = \mathrm{atan2}\left(u_{\mathrm{cos},\{\mathrm{S1,S2}\}}, u_{\mathrm{sin},\{\mathrm{S1,S2}\}}\right), \qquad (21)$$

whereas the linear position is calculated from the amplitude as

$$z_{\{\mathrm{S1,S2}\}} = f_{\mathrm{fit}}\left(\sqrt{u^2_{\mathrm{sin},\{\mathrm{S1,S2}\}} + u^2_{\mathrm{cos},\{\mathrm{S1,S2}\}}}\right), \qquad (22)$$

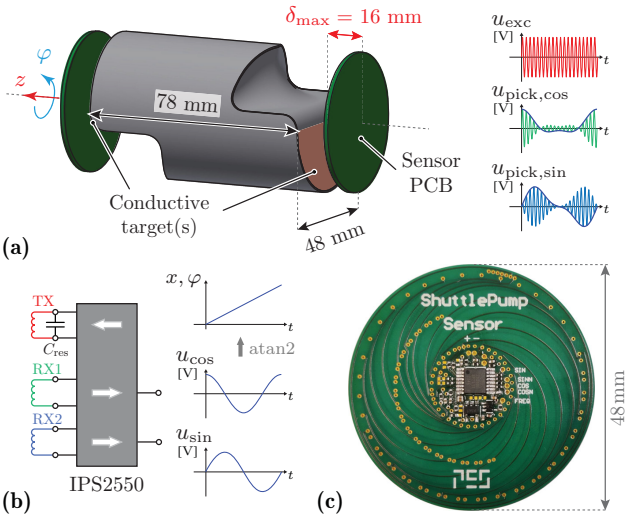

FIGURE 19. *ShuttlePump* linear-rotary position sensors [18]. **(a)** Placement of the PCB-embedded ECSs with respect to the piston of the *ShuttlePump*, equipped with thin $0.5\,\mathrm{mm}$ highly conductive copper targets placed on the outer axial surfaces. **(b)** ECS interface *IPS2550* by *Renesas*, used to excite the ECS and demodulate the voltages induced in the pick-up coils $u_{\mathrm{pick,cos}}$ and $u_{\mathrm{pick,sin}}$ to obtain the voltages $u_{\cos}$ and $u_{\sin}$. These are then used ti calculate the linear and rotary positions according to (22) and (21). **(c)** Multi-layer PCB realization of the sensor.

TABLE 5. Linear-Rotary ECS measurement results [18].

Linear/Axial Position		Rotary/Angular Position	
z-sensitivity	1.42 - 0.16 V/mm	φ-error (max)	3.75 - 7 °
z-resolution	3.39 - 30 µm		
z-bandwidth	10 kHz	φ-bandwidth	10 kHz

where f is the inverse of a fitted exponential calibration function.

The used ECS interface is the *IPS2550* by *Renesas*, which offers in a single IC one driving channel for the excitation coil and two demodulation channels for the two induced voltages, together with many programmable utilities. The final achieved linear and rotary position resolutions (using a 10-bit ADCs) are reported in **Tab. 5**.

C. POST-PROCESSING OF THE MEASUREMENT SIGNALS

As mentioned in the previous section, the measured signals from the two ECSs are combined to obtain a final measurement of the linear position z_{meas} and the rotary position φ_{meas}. To always use the higher quality signals measured by the sensor with the closest target, the simplest approach is to use a linear weighting of the form

$$z_{\mathrm{meas}} = (8\,\mathrm{mm} - z_{\mathrm{S1}})(1 - w_{\mathrm{z}}) - (8\,\mathrm{mm} + z_{\mathrm{S2}})\,w_{\mathrm{z}}, \qquad (23)$$

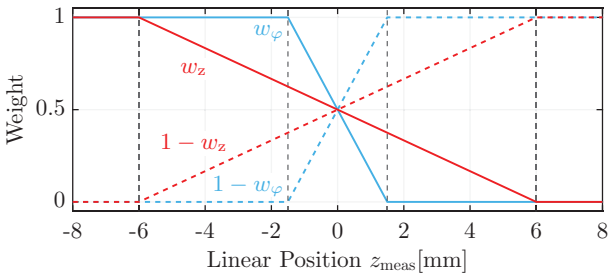

FIGURE 20. Weights w_z and w_φ, as well as the curves $(1-w_z)$ and $(1-w_\varphi)$, used to linearly combine the sensors signals $z_{\{S1,S2\}}$ in (22) and $\varphi_{\{S1,S2\}}$ in (21). The weights w_z and w_φ are calculated according to (24) with $z_{\text{comb}} = 6\,\text{mm}$ and $z_{\text{comb}} = 1.5\,\text{mm}$, respectively.

with the weight w_z depending on the (previous-step) axial position defined as

$$w_z = \begin{cases} 1, & \text{for } z_{\text{meas}} \leq -z_{\text{comb}} \\ \frac{z_{\text{comb}} - z_{\text{meas}}}{2\, z_{\text{comb}}}, & \text{for } -z_{\text{comb}} < z_{\text{meas}} < z_{\text{comb}} \\ 0 & \text{for } z_{\text{meas}} \geq z_{\text{comb}} \end{cases}, \tag{24}$$

where z_{comb} defines the axial position range $[-z_{\text{comb}}, z_{\text{comb}}]$ for which the sensors measurements are linearly combined. In the presented results, $z_{\text{comb}} = 6\,\text{mm}$ is used, and the resulting weight w_z is shown in **Fig. 20**. As mentioned in **Sec. VI**, this post-processing method could introduce measurement disturbances especially around the zero-crossings of the linear position, which can be significant if the calibration is not performed correctly.

For what concerns the rotary angle φ_{meas}, the output angles $\varphi_{\{S1,S2\}}$ calculated by (21) are in the range $[-\pi, \pi]$, so they are first conditioned to $[0, 2\pi]$. Then, the same weighting method as for z_{meas} is used, hence

$$\varphi_{\text{meas}} = (1 - w_\varphi) \cdot \varphi_{S1} + w_\varphi \cdot (\varphi_{S2} - \varphi_{\text{mis}}), \tag{25}$$

with w_φ calculated according to (24) with $z_{\text{comb}} = 1.5\,\text{mm}$ as visible in **Fig. 20**. This value proved to yield the best results experimentally. Finally, the misalignment correction offset φ_{mis} is also a crucial parameter, as the sensors might still provide a slightly different reading even though care is taken during mounting to adjust their relative position. If this is not carefully selected, a pronounced measurement disturbance appears in the measured rotary angle φ_{meas}, corresponding to the difference $\varphi_{S1} - \varphi_{S2}$.

REFERENCES

[1] R. E. S. Bowen, T. J. Graetz, D. A. Emmert, and M. S. Avidan, "Statistics of Heart Failure and Mechanical Circulatory Support in 2020," *Annals of Translational Medicine*, vol. 8, no. 13, 2020.

[2] R. Hetzer, M. F. del Maria Javier, M. Dandel, M. Loebe, and E. M. J. Delmo, "Mechanical Circulatory Support Systems: Evolution, the Systems and Outlook," *Cardiovascular Diagnosis and Therapy*, vol. 11, no. 1, 2020.

[3] J. L. Vieira, H. O. Ventura, and M. R. Mehra, "Mechanical Circulatory Support Devices in Advanced Heart Failure: 2020 and Beyond," *Progress in Cardiovascular Diseases*, vol. 63, no. 5, p. 630–639, Sep. 2020.

[4] G. Lippi and F. Sanchis-Gomar, "Global Epidemiology and Future Trends of Heart Failure," *AME Medical Journal*, vol. 5, p. 15–15, Jun. 2020.

[5] M. Fuchs, D. Schibilsky, W. Zeh, M. Berchtold-Herz, F. Beyersdorf, and M. Siepe, "Does the Heart Transplant Have a Future?" *European Journal of Cardio-Thoracic Surgery*, vol. 55, pp. i38–i48, 5 2019.

[6] K. S. Shah, M. M. Kittleson, and J. A. Kobashigawa, "Updates on Heart Transplantation," *Current Heart Failure Reports*, vol. 16, no. 5, p. 150–156, Jun. 2019.

[7] A.-H. H. Al Omari, A. V. Savkin, M. Stevens, D. G. Mason, D. L. Timms, R. F. Salamonsen, and N. H. Lovell, "Developments in Control Systems for Rotary Left Ventricular Assist Devices for Heart Failure Patients: A Review," *Physiological Measurement*, vol. 34, no. 1, p. R1–R27, Dec. 2012.

[8] K. Ohuchi, D. Kikugawa, K. Takahashi, M. Uemura, M. Nakamura, T. Murakami, T. Sakamoto, and S. Takatani, "Control Strategy for Rotary Blood Pumps," *Artificial Organs*, vol. 25, no. 5, p. 366–370, May. 2001.

[9] J.-F. Llibre, N. Martinez, P. Leprince, and B. Nogarede, "Analysis and Modeling of Linear-Switched Reluctance for Medical Application," *Actuators*, vol. 2, no. 2, p. 27–44, Apr. 2013.

[10] K. Fukunaga, A. Homma, A. Funakubo, E. Tatsumi, Y. Taenaka, S. Kitamura, and Y. Fukui, "Pulsatile Blood Pump with a Linear Drive Actuator," *Journal of Artificial Organs*, vol. 10, no. 2, p. 77–84, Jun. 2007.

[11] H. S. Zad, T. I. Khan, and I. Lazoglu, "Design and Analysis of a Novel Bearingless Motor for a Miniature Axial Flow Blood Pump," *IEEE Transactions on Industrial Electronics*, vol. 65, no. 5, p. 4006–4016, May. 2018.

[12] J. J. Lee, C. B. Ahn, J. Choi, J. W. Park, S.-J. Song, and K. Sun, "Development of Magnetic Bearing System for a New Third-Generation Blood Pump," *Artificial Organs*, vol. 35, no. 11, p. 1082–1094, Nov. 2011.

[13] Y. Pya, J. Maly, M. Bekbossynova, R. Salov, S. Schueler, B. Meyns, Y. Kassif, M. Massetti, M. Zilbershlag, and I. Netuka, "First Human Use of a Wireless Coplanar Energy Transfer Coupled with a Continuous-flow Left Ventricular Assist Device," *The Journal of Heart and Lung Transplantation*, vol. 38, no. 4, pp. 339–343, 2019.

[14] M. Granegger, T. Bierewirtz, M. Nicolai, and U. Kertzscher, "Blood Pump," EU Patent WO/2022/049166, Mar 10, 2022.

[15] T. Bierewirtz, K. Narayanaswamy, R. V. Giuffrida, T. Rese, D. Bortis, D. Zimpfer, J. W. Kolar, U. Kertzscher, and M. Granegger, "A Novel Pumping Principle for a Total Artificial Heart," *IEEE Transactions on Biomedical Engineering*, vol. 71, no. 2, pp. 446–455, 2024.

[16] R. V. Giuffrida, R. Senti, J. W. Kolar, T. Bierewirtz, K. Narayanaswamy, M. Granegger, and D. Bortis, "Design and Realization of a Highly-Compact Tubular Linear Actuator for a Novel Total Artificial Heart," *IEEE Journal of Emerging and Selected Topics in Industrial Electronics*, 2023.

[17] R. V. Giuffrida, R. Senti, D. Bortis, T. Bierewirtz, K. Narayanaswamy, M. Granegger, and J. W. Kolar, "Spatially Highly Constrained Auxiliary Rotary Actuator for a Novel Total Artificial Heart," *IEEE Open Journal of the Industrial Electronics Society*, vol. 4, pp. 732–747, 2023.

[18] R. V. Giuffrida, J. W. Kolar, and D. Bortis, "Eddy-Current Linear-Rotary Position Sensor for an Implantable Total Artificial Heart," in *Proc. of the 25th International Conference on Electrical Machines and Systems (ICEMS)*, pp. 1–6. IEEE, 2022.

[19] R. V. Giuffrida, S. Mirić, A. Horat, D. Bortis, and J. W. Kolar, "Control System Design and Experimental Verification of a Self-Bearing Double-Stator Linear-Rotary Actuator," in *Proc. of the 13th International Symposium on Linear Drives for Industry Applications (LDIA)*, pp. 1–6, 2021.

[20] S. Mirić, R. Giuffrida, D. Bortis, and J. W. Kolar, "Dynamic Electromechanical Model and Position Controller Design of a New High-Precision Self-Bearing Linear Actuator," *IEEE Transactions on Industrial Electronics*, vol. 68, no. 1, pp. 744–755, 2020.

[21] Z. Ping, T. Wang, Y. Huang, H. Wang, J.-G. Lu, and Y. Li, "Internal Model Control of Pmsm Position Servo System: Theory and Experimental Results," *IEEE Transactions on Industrial Informatics*, vol. 16, no. 4, pp. 2202–2211, 2019.

[22] Plexim GmbH, PLECS Standalone, Plexim GmbH, 2023, version 4.7.1. [Online]. Available: www.plexim.com/products/plecs/plecs_standalone

[23] S. Skogestad and I. Postlethwaite, Multivariable Feedback Control: Analysis and Design, vol. 2. Wiley New York, 2007.

[24] A. Visioli, "Anti-windup Strategies," in Practical PID Control, ser. Advances in Industrial Control, pp. 35–60. London: Springer, 2006.

[25] A. Lagrioui and H. Mahmoudi, "Speed and Current Control for the PMSM Using a Luenberger Observer," in *Proc. of the IEEE International Conference on Multimedia Computing and Systems*, pp. 1–6. IEEE, 2011.

[26] D. Luenberger, "Observers for Multivariable Systems," *IEEE Transactions on Automatic Control*, vol. 11, no. 2, pp. 190–197, 1966.

[27] L. Xiaoquan, L. Heyun, and H. Junlin, "Load Disturbance Observer-based Control Method for Sensorless Pmsm Drive," *IET Electric Power Applications*, vol. 10, no. 8, pp. 735–743, 2016.
[28] W.-H. Chen, J. Yang, L. Guo, and S. Li, "Disturbance-observer-based Control and Related Methods — An Overview," *IEEE Transactions on Industrial Electronics*, vol. 63, no. 2, pp. 1083–1095, 2015.
[29] W.-H. Chen, "Disturbance Observer Based Control for Nonlinear Systems," *IEEE/ASME Transactions on Mechatronics*, vol. 9, no. 4, pp. 706–710, 2004.
[30] L. Xin, Z. Dong, Z. Pei, and W. Rui, "The Current Feedforward Compensation Method for the Cogging Torque of Permanent Magnet Synchronous Motors," in *Proc. of the IEEE 9th Annual International Conference on CYBER Technology in Automation, Control, and Intelligent Systems (CYBER)*, pp. 1091–1095, 2019.
[31] K. C. Yeo, G. Heins, F. De Boer, and B. Saunders, "Adaptive Feedforward Control to Compensate Cogging Torque and Current Measurement Errors for Pmsms," in *Proc. of the IEEE International Electric Machines & Drives Conference (IEMDC)*, pp. 942–947, 2011.
[32] LinMot, "Linear Motors P01-23X80," Datasheet. [Online]. Available: shop.linmot.com/data/import/Dokumente/0185-1000-E_1V1_DS_Linear_Motors_P01-23x80.pdf
[33] LinMot, "Servo Drive B1100," Datasheet. [Online]. Available: https://shop.linmot.com/data/import/Dokumente/0185-1019-E_16V3_DS_Drive_Series_B1100.pdf